Three-dimensional Simulations of an Internal Solitary Wave Shoaling Over a Shallow Slope

by

Nicolas Castro-Folker

A thesis
presented to the University of Waterloo
in fulfillment of the
thesis requirement for the degree of
Master of Mathematics
in
Applied Mathematics

Waterloo, Ontario, Canada, 2022

Author's Declaration

I hereby declare that I am the sole author of this thesis. This is a true copy of the thesis, including any required final revisions, as accepted by my examiners.

I understand that my thesis may be made electronically available to the public.

Abstract

The transport of sediment is vital for ecological and climatological processes. Sediment can either move up the shelf, or mix into the upper water column as nepheloid layers. Internal solitary waves (ISWs) shoaling along sloped beds produce structures and currents that transport sediment. The geometry of the wave and the bed influence the total flux due to this transport, and whether or not the sediment forms nepheloid layers. Both numerical and experimental investigations, at both the field and laboratory scales, have been conducted with the goal of understanding the aforementioned relationship. Though these investigations have a common goal, they approach it from differing perspectives. Some focus on the mechanisms behind the ejection of sediment from the bottom boundary layer (BBL); others focus on the sub-processes of shoaling; some report on the coincidence of sediment and wave events in natural systems; others perform experiments that directly study the interactions between waves and sediment.

This thesis describes three-dimensional, laboratory-scale DNS of an internal solitary wave of depression (ISW-D) shoaling over a shallow linear slope ($S \approx 0.05$); it is primarily concerned with describing the sub-processes of shoaling waves. The amplitude and width of the initial waves are chosen so that the systems remain in the fission regime. An ISW-D in this regime steepens, fissions into a nonlinear wave train, and forms a train of boluses; as the wave does so, it interacts with the BBL to produce instabilities. Each stage has qualitatively different instabilities, though of particular interest are vortices induced by BBL instabilities during wave fission. The initial stages of the shoaling process, and the instigation of pycnocline overturning are found to be two-dimensional. Additionally, once three-dimensionalization does occur, it does so through independent processes during the transition from the fission phase to the bolus phase, and once again during the degeneration of the bolus. Implications for mixing, and sediment advection in coastal contexts are discussed.

Acknowledgements

I'd like to thank my supervisor, Marek Stastna, for putting up with a writing process that could cleanse souls in purgatory. I'd also like to thank my family for their support and encouraging words whenever I wanted to retreat to a life of scrounging and banjo in the backwoods of Nova Scotia.

Finally, I'd like to thank Taylor Hanson, Aaron Coutino, and Marek Stastna for lending me a data set for demonstrative purposes. They use said data in their paper, *Stratified shear instability in the cabbeling regime* [18].

Dedication

To my friends, Ashton, Ethan and Ben, without whom I would not have left my house once during my degree. And, to my dogs, Jack and Sam, who will never read this but get the gist. And, in the off–chance she sees this, to Mitski.

Table of Contents

List of Figures

List of Tables

Chapter 1

Introduction

Solitary waves are localized disturbances that maintain their form as they propagate. They were first observed by Russell and a colleague in the middle of the 19$^{\text{th}}$ century [35]. In the hydrodynamic context they manifest as both surface waves and, if the fluid is stratified, internal waves. As internal waves, they travel along density contours, and are frequently observed in lakes, and coastal oceans [7, 23, 27]. By definition, solitary waves maintain their form as they propagate, but, in natural systems, dispersion, aeolian forcing, tidal forcing, wave-wave interactions, and wave-boundary interactions cause them to degenerate into complex systems of nonlinear waves [27]. Accordingly, while the waves can be observed directly, they can also be identified by structures produced during their degeneration, such as trains of nonlinear waves, sand ripples along the coastal shelf, clouds of sediment in the water column (nepheloid layers), and shoreward surges of dense fluid that travel along the bottom boundary [7, 27]. The evolution and degeneration of these waves and associated structures are central to the dissipation of planetary energy [20], as well as mineral and nutrient cycles [7], and are thus discussed extensively in the literature.

Natural stratifications and bathymetries are complex and change with seasons and geographical location [20, 27]. The large disparity between the wave scale and the scale at which viscous dissipation takes place is also a complicating factor in natural environments. As such, several scaled-down and simplified systems are used to study shoaling waves in the experimental and theoretical literature. The most common stratifications are quasi-two-layer stratifications (that is, stratifications with two homogoneous layers separated by a sharp transition region), (piecewise) linear stratifications, and continuous nonlinear stratifications [20]. Additionally, common domains include level rectilinear tanks [36], tilted rectilinear tanks [46], level rectilinear tanks with finite hills [34, 47], level tanks with linear ramps [1, 2, 4, 43], and level tanks with complex hills that mimic the rapid

change in slope at the continental shelf break [32, 42]. Broadly speaking, all lab-scale investigations show a similar evolution for shoaling waves of depression: an incident wave steepens, breaks, and subsequently produces pulsed surges of dense fluid known as boluses. Adjusting the parameters of the initial wave, the stratification, or the domain geometry, however, changes the specifics of wave breaking and bolus formation (and thus the specifics of turbulent mixing and the potential for sediment transport) [1, 2, 4, 7, 27, 32, 42, 46]. Accordingly, a major objective is to understand and classify the changes to these specifics in terms of the domain and wave parameters.

Linear–slope experiments work towards this objective by classifying systems according to the relative steepness of the wave[1] to the slope of either a linear ramp in a level tank, or to slope of the tank bottom if the domain is tilted. While the bathymetry of a system like the continental shelf is more complex than a linear slope, the shallow angles and size of natural internal solitary waves mean such an idealization is not a poor first approximation. For further simplicity, many linear-slope experiments use single-component, quasi-two-layer stratifications. As such, physical experiments are often analyzed using parameters and notions from weakly nonlinear theory (henceforth WNL), often applied to strictly two-layer systems; examples of these parameters will be discussed in Chapter 2. In sloped, quasi-two-layer systems, the height of the *pycnocline*[2] above the bottom decreases across the domain. In most configurations, the pycnocline changes from resting above mid-depth to resting below mid-depth. Exact internal solitary wave theory, or DJL theory, then implies that an initial internal solitary wave of depression (henceforth ISW-D) should reverse its polarity (that is, become a wave of elevation) when waves pass the point at which the pycnocline is at the mid-depth (henceforth transition point) [7, 32]. The reversal in polarity, combined with sufficient nonlinear steepening that increases with the domain slope, can cause the wave to break at, or near, the transition point [2, 7, 32]. This does not always occur; if the domain slope is shallow, then steepening is slight, and the wave fissions into a wave train instead. Despite the relatively gentle wave evolution, the fissioning case leads to instabilities in the bottom boundary layer that can in turn induce breaking [46, 17]. The wave breaking and fissioning situations represent two poles on the spectrum of linear-slope experiments. The qualitative differences between these scenarios and their intermediates have implications for turbulent mixing, bolus characteristics, and potential for sediment resuspension and transport [4, 7, 27, 17].

Much of the linear-slope literature from 1980 to 2010 investigates laboratory-scale shoaling ISWs using 1m-5m long tanks tilted at steep angles [7, 27]. This is due to technological

[1] This is roughly equivalent to the aspect–ratio of the wave.

[2] The sharp transition region in the density field.

limitations, as realistic systems[3] are on the order of tens of kilometres long, and have very slight angles of inclination [7]. Most laboratories are, due to spatial limitations, unable to use tanks longer than the length of a swimming pool; however, by appropriately scaling the amplitude and width of the wave, they can get away with using shorter tanks. It is then (in principle) simple for an experimentalist to control the angle of the slope, as they can use ramps either inside or outside the tank to arbitrarily adjust the angle of inclination. At this point, the experimentalist is only limited by the sensitivity of their probes (e.g., some ADVP probes are known to have trouble resolving the bottom boundary layer (henceforth BBL) [17]). Nonetheless experimentalists are able to make accurate observations of these systems; it is then the job of the numericist to provide precise observations via high-resolution simulations of the laboratory systems. Numericists, are limited even more by technology, and it can take years to have the computational resources to exactly simulate an experimental set-up. For instance, in 1988, Wallace and Wilkinson [43] were able to perform sloped experiments in an 18m long tank (12m were flat, and 6m were sloped), and then, in 2014, Arthur and Fringer [4] were able to perform three-dimensional direct numerical simulations (henceforth DNS) of similar, slightly shorter systems (their longest domain was flat for 1.675m, and sloped for 11m)[4]. Now, these statements are not meant to unduly criticize the work of earlier experimentalists or numericists; indeed, the narrative of linear–slope systems discussed above was only made possible by the rigorous and detailed work of earlier scholars. The statements are meant to showcase the limitations they faced, and to motivate the direction of present linear–slope work: three-dimensional DNS of long tanks with extremely shallow angles of inclination.

As stated above, recent work uses longer tanks and shallower angles. This allows the wave to fission, and it also draws out the fissioning process so researchers can observe the turbulence generated by the BBL instabilities of the shoaling wave-train. Until the 2010s, DNS of shoaling systems has been mostly restricted to two dimensions, but modern studies by Arthur and Fringer [4], Xu et. al. [47], Olsthoorn and Stastna [34], Sakai et. al. [36], and Hartharn-Evans et. al. [20] have extended investigations into three dimensions. A general theme is that wave-breaking on steep slopes, mixing, sediment deposition, and bolus degeneration are three-dimensional [4, 34]. Accurate accounting of energetics and mass-flux therefore requires DNS of fully three-dimensional systems. On the other hand, two-dimensional simulations using shallow slopes reveal mechanisms that generate vortices capable of breaking the wave and producing boluses, suggesting that some significant sub-processes can only be approximately understood in just two dimensions. Of course, this notion can only be confirmed by contrasting two-dimensional systems to their

[3] In this thesis, this is taken to mean systems that mimic the geometry of the coastal shelf.

[4] As an aside, by using a longer sloped portion, they were able to observe more of the shoaling process.

three-dimensional extensions.

The present work is concerned with three-dimensional direct numerical simulations of ISW-Ds in a quasi-two layer, single-component fluid shoaling on a shallow, linear slope. The resolution of the simulations and accuracy of the high-order, pseudo-spectral solver allow for detailed, qualitative descriptions of the instabilities triggered by, and the coherent structures formed during, the shoaling process. Chapter 2 provides an explanation of technical details with discussions regarding: using the several assumptions (including the assumption of the validity of the Boussinesq approximation) to derive the incompressible Navier-Stokes equations from the local conservation equations of momentum, mass, and thermal energy; the pseudo-spectral numerical solver used in this investigation, SPINS, and its alternatives; the initial conditions, boundary conditions, and the domain set-up; the parameters used to characterize ISWs and slopes, and the experimental cases used in this investigation; bed-stresses and how they are used to estimate sediment advection; and, finally, a note on the identification and visualization of coherent vortices using the λ_2 criterion of Jeong and Hussain [24]. Chapter 3 is a report on the results of the simulations performed. Briefly, the results are that the evolution has three qualitatively distinct phases (wave incidence, fission, and bolus formation), and that these phases produce three sets of qualitatively distinct instabilities (a prograde jet, a separation bubble, and lobe-cleft and shear instabilities). The results highlight the relationship between the wave amplitude and the instability intensity, and between the amplitude and the emergence of spanwise variation. The boundary layer stresses are also described. A summarization of the narrative finishes the chapter. The final section, Chapter 4, begins with a discussion contextualizing the results within the broader literature, and ends with a brief speculation on future laboratory-scale work, such as investigations with sediment–coupled models, and investigations focused on the quantitative analysis of mixing and dissipation.

Chapter 2

Numerical Methods and Technical Background

2.1 The Governing Equations

Fluid dynamics describes changes in fluid mass density (ρ), flow velocity ($\vec{u} = (u, v, w)$), internal pressure (p), Temperature (T), and occasionally concentrations of chemicals (n_i, where i is the index label of the chemical), due to conservative external forces and internal processes. Any model of a fluid requires a system of equations that governs the evolution of these variables, as well as an equation of state that expresses ρ as a function of p, T, and—if applicable—n_i; in simple cases, among which the present investigation is included, n_i is ignored, and we can write

$$\rho = f(p, T), \tag{2.1}$$

as the equation of state. The evolution equations used in this investigation will be the famous incompressible Navier-Stokes equations (henceforth the NS equations).

A standard topic in an introductory fluid mechanics course is the derivation of the NS equations from the equations for the local conservation of mass, momentum, and thermal

energy; Kundu and Cohen [26] present these conservation equations as

$$\frac{1}{\rho}\frac{D\rho}{Dt} + \vec{\nabla}\cdot\vec{u} = 0, \tag{2.2}$$

$$\rho\frac{D\vec{u}}{Dt} + \frac{D\rho}{Dt}\vec{u} + (\vec{\nabla}\cdot\vec{u})\rho\vec{u} = \vec{\nabla}\cdot\tau - \vec{\nabla}\pi, \tag{2.3}$$

$$\frac{De}{Dt} = -\vec{\nabla}\cdot\vec{q} - p\vec{\nabla}\cdot\vec{u} + \phi, \tag{2.4}$$

respectively. In the above expressions, $\frac{D}{Dt} = \partial_t + \vec{u}\cdot\vec{\nabla}$ is the material derivative, ∂_t is the partial derivative with respect to time, τ is the internal stress tensor, π is the scalar potential due to external body forces, e is the internal thermal energy density, $\vec{q}$ is the heat flux, and

$$\phi = 2\mu S_{ij}S_{ij} - \frac{2}{3}\mu u_{i,i}$$

is the rate of viscous dissipation (i.e., the rate at which useful energy is irreversibly converted to heat by internal friction).

Following the example of Kundu and Cohen [26], several simplifying assumptions will be used to derive the NS equations from Equations 2.2-2.4. More involved derivations (that nonetheless make some of the same assumptions) can be found in Spiegel and Veronis [37], and in Batchelor [6].

The first assumption is that the fluid is Newtonian. That is, the stress tensor is assumed to obey the following constitutive equation [26]:

$$\tau_{ij} = -\left(p + \frac{2}{3}u_{k,k}\right)\delta_{ij} + 2\mu S_{ij}, \tag{2.5}$$

where μ is the dynamic viscosity, δ_{ij} is the Kroenecker delta, and $S_{ij} = \frac{1}{2}(u_{i,j} + u_{j,i})$ is the rate of strain tensor. Note that the Einstein summation convention is used, and that $u_{i,j} = \partial_j u_i$ where ∂_j is the partial derivative with respect to the j^{th} Cartesian coordinate.

The next assumption is that surface gravity is the only body force acting on the fluid:

$$-\vec{\nabla}\pi = \rho\vec{g}, \tag{2.6}$$

where $\vec{g}$ is the gravitational acceleration. Substituting Equations 2.2, 2.5, and 2.6 into Equation 2.3 gives

$$\rho\frac{D\vec{u}}{Dt} = -\vec{\nabla}\left(p - \frac{1}{3}\mu\vec{\nabla}\cdot\vec{u}\right) + \rho\vec{g} + \mu\nabla^2\vec{u}. \tag{2.7}$$

The third assumption is that the fluid is an ideal gas that obeys Fourier's heat law. This assumption is made by both Spiegel and Veronis [37], and by Kundu and Cohen [26]. Some readers may object to the 'ideal gas' portion of the assumption, since this thesis is concerned with modelling oceanographic processes, and the ocean is very much not an ideal gas. Indeed, a more general approach is employed by Batchelor [6] in his text. Nonetheless, the ideal gas assumption allows for a simple and concise derivation, which is conducive to clear exposition. With this in mind, the third assumption gives the following relations [26, 37]:

$$\begin{aligned} \frac{De}{Dt} &= C_v \rho \frac{DT}{Dt} \\ p\vec{\nabla} \cdot \vec{u} &= (C_p - C_v)\rho \frac{DT}{Dt}, \\ \vec{q} &= -k\vec{\nabla}T, \end{aligned}$$

where C_p is the isobaric heat capacity, C_v is the volumetric heat capacity, and k is a proportionality constant. Substituting these relations into 2.4 eliminates e and q from the thermal energy equation, and yields

$$\gamma \frac{DT}{Dt} = k\nabla^2 T + \phi, \tag{2.8}$$

with $\gamma = \rho C_p$. The thermal diffusivity of the fluid is then defined as $\kappa = k/\gamma$. This is not necessarily constant because of the dependence on ρ.

The final assumption is that the Boussinesq approximation is valid. This is true of systems where thermal[1] fluctuations are small, and where the effects of pressure waves are negligible. Formally, this latter condition means

1. If U is a characteristic speed of the flow, and c is the speed of sound in the fluid, then the Mach number, $M = U/c$, must satisfy $M < 1.3$ [26]; that is, the effects of sound waves are negligible.

2. $L_z \ll D$, where D is a length scale over which density changes appreciably due to pressure in the overlying fluid column[2] [26, 37]

3. The change in density over L_z ($\Delta\rho$)is negligible compared to the static domain–averaged density (ρ_0): $|\Delta\rho/\rho_0| \ll 1$ [37]

[1] Or chemical.

[2] e.g., this would not be satisfied at the bottom of the ocean.

If these conditions hold, then the approximation posits that

1. Density fluctuations are due solely to thermal fluctuations[3]
2. The resultant fluctuations in density are negligible relative to the magnitude of the density, except in the buoyancy term of the momentum equation

The second posit implies the inequality,

$$\left|\frac{1}{\rho}\frac{D\rho}{Dt}\right| \ll |\vec{\nabla}\cdot\vec{u}|,$$

which in turn implies

$$\boxed{\vec{\nabla}\cdot\vec{u}\approx 0}$$

when applied to Equation 2.2. That is, fluids for which the Boussinesq approximation is valid are *incompressible*. This incompressibility immediately leads to a simplification of Equation 2.7,

$$\rho\frac{D\vec{u}}{Dt} = \vec{\nabla}p + \rho\vec{g} + \mu\nabla^2\vec{u}. \tag{2.9}$$

Additionally, the viscous dissipation, ϕ, is also simplified [26]:

$$\phi = 2\mu S_{ij}S_{ij}.$$

Dimensional analysis then implies

$$\left|\frac{\phi}{\gamma\frac{DT}{Dt}}\right| = \left|\frac{2\mu S_{ij}S_{ij}}{C_p\rho\frac{DT}{Dt}}\right| \sim \frac{\nu U}{C_p\delta T L} \ll 1,$$

where U is a characteristic velocity, L is a characteristic length, $\nu = \mu/\rho$ is the kinematic viscosity, and δT is a characteristic variation in temperature. That is, ϕ can be ignored[4], and Equation 2.8 becomes

$$\frac{DT}{Dt} = \kappa\nabla^2 T. \tag{2.10}$$

[3] If fluctuations in chemical concentrations are present, as in a double-diffusive system, then they also contribute to density. In any case, the supposition is that density variations due to pressure fluctuations are negligible compared to density variations due to fluctuations of the other intensive state variables.

[4] Indeed, this ratio is approximately 10^{-11} using the parameters in Tables 2.1 and 2.2.

Next, decompose the density as

$$\rho(\vec{x}, t) = \rho_0 + \rho'(\vec{x}, t),$$

where ρ_0 is the same variables defined above, and ρ' contains all the fluctuations. Suppose there exists a static fluid with uniform density ρ_0. The pressure in the hypothetical static fluid, $p_0(\vec{x})$, would satisfy

$$\vec{\nabla} p_0 = -\rho_0 \vec{g},$$

so substituting the resultant pressure decomposition,

$$p(\vec{x}, t) = p_0(\vec{x}) + p'(\vec{x}, t),$$

and the density decomposition into the momentum equation yields

$$\left(1 + \frac{\rho'}{\rho_0}\right) \frac{Du}{Dt} = -\frac{1}{\rho_0} \vec{\nabla} p' - \frac{\rho'}{\rho_0} \vec{g} + \nu \nabla^2 \vec{u}.$$

In the above, the hydrostatic pressure and density terms have cancelled each other out, and $\nu = \mu/\rho_0$ is now constant. The second posit of the Boussinesq approximation, $|\rho'/\rho_0| \ll 1$, further simplifies the momentum equation to

$$\boxed{\frac{Du}{Dt} = -\frac{1}{\rho_0} \vec{\nabla} p' + \frac{\rho'}{\rho_0} \vec{g} + \nu \nabla^2 \vec{u}.}$$

As stated earlier, the buoyancy term still retains a factor of ρ'/ρ_0. Kundu and Cohen [26] explain this heuristically by noting that gravity is the sole external force, and therefore has a magnitude comparable to the magnitudes of shear-stress term ($\nu \nabla^2 \vec{u}$) and the acceleration term ($\frac{\partial \vec{u}}{\partial t}$).

The Boussinesq approximation can be used to further simplify the energy equation. Once again, the second assumption of the Boussinesq approximation yields

$$\rho'/\rho_0 \ll 1 \Rightarrow \gamma = \left(1 + \frac{\rho'}{\rho_0}\right) \rho_0 C_p \approx \rho_0 C_p,$$

so κ is a constant with the same units as ν. More significantly, as a direct result of the first assumption in the Boussinesq approximation,

$$\rho' = f(T'),$$

where T' represents fluctuations about a static T_0 defined by the equation of state for the hydrostatic system discussed above. Because the fluid is an ideal gas, the dynamic system obeys

$$p = a\rho T,$$

and the static system obeys

$$p_0 = a\rho_0 T_0,$$

where a is a proportionality constant. Consequently,

$$\begin{aligned}
\rho_0 + \rho' &= f(T_0, p_0) + \frac{\partial f}{\partial T}(T_0, p_0)T' + \frac{\partial f}{\partial p}(T_0, p_0)p' + O(T'p'), \\
&= \rho_0 - \frac{p_0}{T_0^2}T' + \frac{1}{aT_0}p' + O(T'p'), \\
&\approx \rho_0 - \frac{p_0}{T_0^2}T' + \frac{1}{aT_0}p', \quad \text{[Fluctuations are slight relative to } \rho_0\text{]} \\
&\approx \rho_0 - \frac{p_0}{T_0^2}T', \quad \text{[By first posit of the Boussinesq approximation]}
\end{aligned}$$

That is, $\rho' \propto T'$, and therefore

$$\boxed{\frac{D\rho}{Dt} = \kappa\nabla^2\rho}$$

immediately follows from equation 2.10, the advection-diffusion equation for T.

All told, the conservation equations have become the familiar incompressible Navier-Stokes equations with diffusion.

$$\frac{D\vec{u}}{Dt} = -\frac{1}{\rho_0}\vec{\nabla}p + \frac{\rho}{\rho_0}\vec{g} + \nu\nabla^2\vec{u}, \tag{2.11}$$

$$\vec{\nabla}\cdot\vec{u} = 0, \tag{2.12}$$

$$\frac{D\rho}{Dt} = \kappa\nabla^2\rho. \tag{2.13}$$

Note that the primes on the density and pressure terms have been dropped for simplicity.

In the present investigation, the x-axis has a streamwise orientation and is aligned with the floor of the tank, the z-axis is normal to (and points out of) the floor of the tank, and the y-axis is then aligned according to the right-hand rule. The tank is tilted at an angle θ relative to the surface of the Earth, so

$$\vec{g} = -g(\sin(\theta)\hat{i} + \cos(\theta)\hat{k}), \tag{2.14}$$

where $\hat{i}$ is the unit vector aligned with the x–axis, and $\hat{k}$ is the unit vector aligned with the z–axis. For a visual reference, see Figure 2.1.

2.2 Numerical Methods and Simulation Configuration

2.2.1 Numerical Model

Equations 2.11-2.13 are solved using the psuedo-spectral collocation method implemented in the software library SPINS. SPINS was developed by Christopher Subich in his PhD thesis [39]. Since then, this model has been under active development by the original author and members of the Environmental and Geopshyical Fluid Dynamics group in the Applied Mathematics Department of the University of Waterloo. Briefly, the model discretizes spatial fields using an implementation of collocation, and it discretizes time using a variable time–step, third order Adams-Bashforth method. It uses an exponential filter to rapidly dampen energy at a cut-off length-scale[5], but it can also be configured to use hyperviscosity instead; in the present investigation only the exponential filter is used. Alternatives to SPINS exist for the configuration used in this thesis, for example the method of Cui [4, 12], SUNTANS [16], and MITgcm [31], all of which are finite-volume methods of relatively low order (order is discussed below).

As a mathematical problem, collocation is a form of interpolation. A domain can be discretized into a finite collection of points: e.g., a one–dimensional domain of length 1 can be discretized as $\{x_i = i\Delta x\}_{i=0}^{N}$ with even spacing $\delta_x = 1/N$. Continuing this example, let u be some field variable known at a given time t. This u generates a list of $N+1$ points $\{u_i\} = \{u(x_i)\}$. Then, an N^{th} degree polynomial can be interpolated from this set of points, and this can be used to approximate the smooth function u [8, 39]. SPINS implements derivatives using the fast Fourier transform (henceforth FFT), implmented via the highly scalable FFTW package, as opposed to using matrix-representations of the differential operators in the original space [39].

In order to implement no slip boundary conditions, the grid must be modified to the so–called Chebyshev grid in order to avoid the so–called Runge phenomenon [40]. This clusters points near boundaries. While this restricts the size of the time-step it provides additional resolution for boundary layer problems, such as those studied in this thesis.

The order, and thereby the accuracy of the model, is determined by N. When N is large, a collocation method becomes a pseudo-spectral method. An advantage of collocation methods over finite–element methods is the greater increase in accuracy gained by a given increase in discrete degrees of freedom, N [8, 40]. Another advantage over finite–volume and finite–element methods is the ability to explicitly evaluate the nonlinear advection term on the grid [39]. Conversely, finite–element methods are better at handling domains

[5] In implementation, after a cut-off wavenumnber.

with exotic geometry[6], and they do not suffer from enhanced aliasing and ringing caused by grid-sampling errors[7] [39]. All told, given the typically simple geometry of lab-scale process-based studies, and given the power of modern computers, the speed and accuracy of pseudo-spectral methods make them an excellent choice for investigating problems in idealized geometries, such as those considered in this thesis.

The details of the time–stepping implementation (i.e., the specifics of the implentation of the variable time–step third–order Adams–Bashforth method) are taken as a well–validated aspect of the model used. That being said, it is useful to understand the overall approach SPINS uses to evolve the fluid fields. The simplest way to do this is to outline the idea behind the evolution algorithm with a forwards–backwards Euler method [39]:

$$(1-\nu\nabla^2)\vec{u}^{n+1} = u^n + \Delta t\left(-\frac{1}{\rho_0}\vec{\nabla}\ p^* - \vec{u}^n\cdot\vec{\nabla}\vec{u}^n + \frac{\rho^n}{\rho_0}\vec{g}\right), \tag{2.15}$$

$$(1-\kappa\nabla^2)\rho^{n+1} = \rho^n + \Delta t\left(-\vec{u}^n\cdot\vec{\nabla}\ \rho^n\right). \tag{2.16}$$

The superscript n denotes the discrete time, and Δt is the variable time-step determined by the CFL condition. The RHS of each equation are evaluated explicitly using the fields from the current time-step, and then serve as a forcing terms for their respective LHS. The resulting linear problem is then solved implicitly, and the fields are evolved–this sort of approach is known as a *stiffly-stable* or *mixed implicit-explicit* algorithm.

Note that the system 2.15-2.16 is incomplete, since there is no evolution equation for the pressure, p^*. This is a consequence of incompressibility, which implies that p^* is updated instantaneously. SPINS resolves this issue by replacing 2.15 with the following predictor-corrector method for the velocity fields [39]:

$$\vec{u}^* = \vec{u}^n + \Delta t\left(-\vec{u}^n\cdot\vec{\nabla}\vec{u}^n + \frac{\rho^n}{\rho_0}\vec{g}\right), \tag{2.17}$$

$$\Delta t\frac{1}{\rho_0}\nabla^2 p^* = \vec{\nabla}\cdot\vec{u}^*, \tag{2.18}$$

$$(1-\nu\nabla^2)\vec{u}^{n+1} = \vec{u}^* - \Delta t\frac{1}{\rho_0}\vec{\nabla}p^*. \tag{2.19}$$

Equation 2.17 solves for a predicted velocity, $\vec{u}^*$ that is forced solely by advection and body forces. That is, $\vec{u}^*$ is not influenced by the internal stresses of pressure or viscosity, and

[6] with triangular/tetrahedral elements being capable of discretizing almost any shape

[7] That being said, as long as the smallest features of the physical flow, i.e., the largest wavenumbers of the physical flow, are resolved, then this is not a significant issue.

does not need to be incompressible. The divergence of this predicted velocity then appears on the RHS of Equation 2.18 as the forcing term in a Poisson problem for pressure, p^*. Physically, this is the pressure needed to enforce incompressibility between timesteps n and $n+1$. Indeed, the force derived from p^* is applied to the predicted velocity on the RHS of Equation 2.19 as a 'corrector' term. This scheme follows from Equation 2.15 assuming that i) $\vec{u}^n$ is incompressible, and ii) the discretized ∇^2 and $\vec{\nabla}\cdot$ commute [39]. Assumption ii) holds for a sufficiently large order, and away from the boundaries; complications can arise when accounting for no-slip boundary conditions, but the details are beyond the scope of this thesis.

2.2.2 Initial Conditions, Boundary Conditions, and the Domain

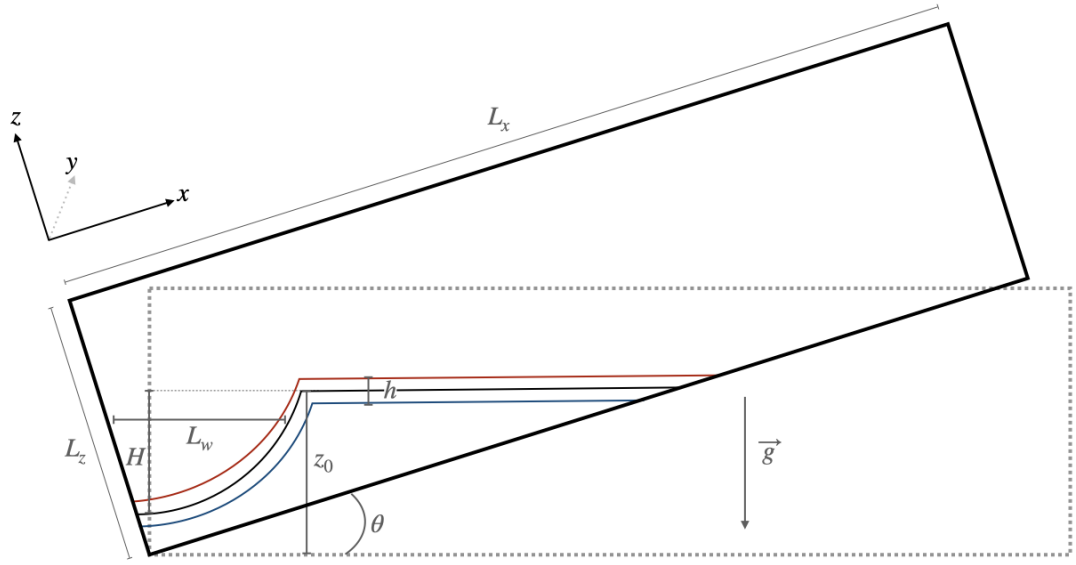

Figure 2.1: A schematic of the initial conditions. The values of the domain parameters can be found in Tables 2.1 and 2.2. The black curved line represents the middle of the pycnocline, and the red (blue) curved line represents the upper (lower) bound of the pycnocline. Note that i) the system is not to scale, and ii) the the cusps in the isopycnals are artifacts of the drawing software used, and the true initial isopycnals are Gaussian curves (see Equation 2.20).

The simulations are intended to mimic a simple laboratory–scale experiment. Namely, they each use a domain that corresponds to a long, tilted, rectilinear flume with a dam–break to initialize the wave. Using a rectilinear domain greatly simplifies the numerics since no mapped grids are necessary. In fact, the only deviation from a standard implementation of Equations 2.11–2.13 was the choice to write gravity as oriented towards the bottom–left of the tank (see Equation 2.14) as opposed to the usual $\vec{g} = -g\hat{k}$.

The initial conditions of the system are given by

$$\rho/\rho_0 = 1 - \frac{\Delta\rho}{2}\tanh\left(\frac{z\cos(\theta) + x\sin(\theta) - H\exp\left(\frac{-x^2}{L_w^2}\right) - z_0}{h}\right), \tag{2.20}$$

$$\vec{u} = 0. \tag{2.21}$$

Equation 2.20 is a thin hyperbolic tangent stratification, where the initial perturbation of the pycnocline has a Gaussian profile. A rough illustration of the domain and the initial conditions can be seen in Figure 2.1. The parameters in Equation 2.20 are: $\Delta\rho$, the bulk, vertical change in density; θ, the angle of inclination; H, the initial amplitude of the Gaussian profile; L_w, the half–width parameter of the Gaussian profile; z_0, the undisturbed height of the pycnocline; and h is the half–width of the pycnocline. The values of these parameters can be found in Tables 2.1 and 2.2.

Though the physical system starts at rest, each component of the simulation initial velocity is additively perturbed with white noise of the form

$$\epsilon_p \chi,$$

at every point in the domain. $\epsilon_p = 10^{-3}$m/s is the magnitude of the perturbation, and χ is a dimensionless random variable that follows a normal distribution with a mean of 0, and a standard deviation of 1. The white noise is added to instigate instabilities by weakly and randomly energizing the velocity fields; this simulates the random environmental fluctuations that would perturb the fluid in a physical tank.

$\Delta\rho$	L_w	h	z_0	ρ_0
(-)	(cm)	(cm)	(cm)	(kg/m^3)
0.02	25.0	1.2	25.0	1000.0

Table 2.1: Parameters used in equation 2.20. With the exception of $\Delta\rho$ and ρ_0, these are visualized in Figure 2.1

The phenomena of interest require an interaction between the wave, topography, and a viscous bottom boundary layer; as such, the velocity fields at the top and bottom of the domain must have no-slip (i.e., homogeneous Dirichlet) boundary conditions. SPINS, the psuedo–spectral solver used in this thesis, implements this via a Chebyshev grid in the z direction. For simplicity, as well as computational efficiency, the velocity fields at the remainder of the boundary obey free-slip (i.e., Neumann) boundary conditions. Finally, velocity obeys the "no-pass" condition and density obeys the "no-flux" condition; i.e., they

respectively satisfy $\vec{u}\cdot\hat{n}=0$ and $\vec{\nabla}\rho\cdot\hat{n}=0$ along every boundary, where $\hat{n}$ is the normal of the boundary. As a point of interest, sediment-coupled models, where the sediment is taken to be extremely fine, have been implemented in SPINS by adding an evolution equation for the concentration of sediment, C_s, in addition to a flux-law for C_s at the bottom boundary [34]. Other sediment models use a large eddy simulation (henceforth LES), a quadratic stress law, and a Shields model[8] to represent large-grain sediment dynamics in an Eulerian perspective [34].

In every case, the size of the domain is $L_x \times L_y \times L_z = 8.192\text{m}\times 0.256\text{m}\times 0.300\text{m}$, and it is discretized using a grid with $N_x \times N_y \times N_z = 8192 \times 256 \times 256$ points. This achieves an approximately 1mm resolution across the domain (with a finer resolution near the vertical boundaries, and a courser resolution in the interior), which is competitive with the resolution of recent simulations [4] carried out with second order finite volume codes. This resolution is approximately within 1 order of magnitude of the Kolmogorov length scale, and it does not use a closure model for sub-filter scales, so the simulations are essentially direct numerical simulations (henceforth DNS) [5].

That being said, extreme thinning of the pycnocline during overturning, and during the degeneration of the bolus produces mild, temporary ringing at scales not damped by the exponential filter. The ringing obfuscates any potential mixing calculations. As such, this thesis is focused on the qualitative description of the systems, and uses visualizations of the primary fluid fields and vortices[9] as proxy measurements of mixing.

2.3 Parameters and the Experimental Cases

2.3.1 Wave Parameters

Solitary waves are maintained by a balance of nonlinear steepening and non-hydrostatic dispersion. By definition, nonlinearity is not captured by linear theories such as the shear-free, long-wave[10] Taylor-Goldstein equation. A simple model[11] that does include these

[8] Shields models are discussed in Subsection 2.3.2. Briefly, they experimentally determine a critical bottom stress that when exceeded leads to sediment transport or resuspension at a given Re.

[9] The calculations of the derivatives needed to detect vortices are also, to a lesser degree, obfuscated; nonetheless, the bulk features of the coherent vortices are captured, and only fine details of the vortices are in doubt. Furthermore, these bulk features are all that is needed for a qualitative analysis of the flow.

[10] The long-wave equation simply means that the vertical extent of the domain is much smaller than the horizontal scale of a given wave.

[11] which is one-dimensional in space and evolves in time

effects is the Korteweg-de Vries (henceforth KdV) equation:

$$\frac{\partial \eta}{\partial t} + (c_0 + \alpha\eta)\frac{\partial \eta}{\partial x} + \beta\frac{\partial^3 \eta}{\partial x^3} = 0, \tag{2.22}$$

where η is the isopycnal displacement, c_0 is the linear longwave speed, $\alpha \sim H/L_z$ is the nonlinearity parameter and $\beta \sim (L_z/2L_w)^2$ is the dispersion parameter. These parameters are taken to be small, but finite. In a two-layer system, with no background flow, Helfrich and Melville [21] relate the parameters as follows:

$$c_0 = \left(\frac{g\Delta\rho h_1 h_2}{h_1 + h_2}\right)^{1/2}, \tag{2.23}$$

$$\alpha = \frac{3}{2}c_0\frac{h_1 - h_2}{h_1 h_2}, \tag{2.24}$$

$$\beta = \frac{c_0}{6}h_1 h_2, \tag{2.25}$$

where g is the magnitude of the gravitational acceleration, h_1 is the thickness of the top layer, h_2 is the thickness of the bottom layer, and $\Delta\rho$ is the difference in density between layers. Since the tank is tilted, an estimate is needed for h_1. Following the example of Xu et. al. [46], let

$$h_1 = \frac{z_0 + L_z/2}{2}.$$

This estimates the lower-layer thickness as an average between the height of the pycnocline and half of the domain thickness. The thickness of the upper layer then immediately follows, since $h_2 = L_z - h_1$. These values are used to calculate the c_0 that will be used to define other variables below and in Table 2.2.

A powerful prediction of the KdV theory, is that waves of depression occur when $h_1 > h_2$, and waves of elevation occur when $h_1 < h_2$. To see this, suppose η_D is a wave of depression solution to Equation 2.22 when $h_1 > h_2$. Now, let $\eta_E = -\eta_D$ (i.e., its isopycnals are deflected in the opposite direction of the isopycnals of η_D). Then,

$$\begin{aligned}
&\frac{\partial \eta_E}{\partial t} + (c_0 - \alpha\eta_E)\frac{\partial \eta_E}{\partial x} + \beta\frac{\partial^3 \eta_E}{\partial x^3} \\
=&-\frac{\partial \eta_D}{\partial t} - (c_0 + \alpha\eta_D)\frac{\partial \eta_D}{\partial x} - \beta\frac{\partial^3 \eta_D}{\partial x^3} \\
=&0.
\end{aligned}$$

That is, for each η that solves the KdV with a given α, there exists a solution $-\eta$ that solves the KdV with $-\alpha$ (i.e., where the the heights of the top and bottom layers are

swapped, and both waves are travelling in the same direction). Thus, the KdV equation suggests that, along a linear slope, a wave of depression will switch to a wave of elevation (i.e., switch polarity) at the point where the pycnocline passes mid-depth. This point is known as the *turning point*, and it should not be confused with the *interaction point*, which is where the pycnocline intercepts the slope.

This model is formally only valid in two-layer systems in the weakly nonlinear (henceforth WNL) and weakly dispersive regimes; those restrictions notwithstanding, KdV theory and its extensions into less-weak regimes show good agreement with experimental results [21]. As such, they are used to analyze experimental measurements and estimate parameters such as the below-wave Stokes boundary layer thickness[12] [4, 46],

$$\delta = 2\sqrt{\frac{\nu L_w}{c_0}}, \tag{2.26}$$

and wave Reynolds number,

$$Re_{ISW} = \frac{c_0 H}{\nu}. \tag{2.27}$$

These variables use c_0, which can be calculated with linear theory (e.g., the Taylor-Goldstein equation), but showing that it is also the speed for WNL waves lends credence to its use in estimating parameters for the highly nonlinear systems studied in this thesis.

A WNL theory, by definition, cannot capture the full effects of steepening and breaking[13], since such a theory loses predictive power once the amplitude becomes too large. As such, the study of breaking and degnerating ISWs over a flat bottom, and the study of shoaling waves, requires inferences from exact solutions for the Dubreil Jacotin Long (henceforth DJL) equation [38], or the analysis of a DNS.

The study of shoaling ISWs is largely concerned with classifying experiments by relative wave–slope geometry. In linear–slope experiments, the natural parameter for such classifications is known as the Iribarren number [7],

$$Ir = \frac{\tan\theta}{\sqrt{H/L_w}}. \tag{2.28}$$

It is the ratio of the bed slope to the wave slope. In the limit of $Ir \to \infty$, the bed slope is essentially a vertical plane, in which case the wave is horizontally squeezed and vertically stretched before reflecting; in the opposite limit, the bed slope is essentially flat, in which

[12] This will be used to calculate a bed pseudo-stress, τ_{ISW}, which is defined in the next subsection.
[13] Indeed, the measured speed of the waves is approximately 7cm/s.

case the wave travels past unaltered. This implies that wave energy in large Ir systems is mostly reflected, while wave energy in small Ir systems is mostly transmitted. The resultant differences in the dynamics at the turning point are visualized clearly in Figure 3 from Nakayama et. al. [33], and in Figures 3–5 from Moore et. al. [32].

2.3.2 Bed stresses

A significant motivation for the study of shoaling internal waves and BBL instabilities is to understand their potential for the transport and resuspension of sediment [7]. Early experimental attempts to classify flows based on their resuspension potential used rectilinear channels with nearly uniform flows passing over a layer of sediment [28]. Broadly speaking, experimentalists measure the streamwise current, and the induced streamwise bottom stress,τ_{zx}, and note the threshold currents at which they observe either i) incipient motion in the sediment layer, or ii) the ejection of sediment into the water column. This model assumes parallel shear flow; another approach, concerned solely with resuspension, considers whether or not the vertical velocity within the BBL is capable of overcoming a sediment grain's settling velocity [1]. The stress used for this model, τ_{ISW}, is not a true bed-stress; both it and τ_{xz} are to be precisely defined and discussed below.

These models are known as *Shields models*. They consider the dimensionless quantity

$$\sigma = \frac{\tau_b}{(\rho_s - \rho)gd}, \tag{2.29}$$

where τ_b is a bed stress, ρ_s is the (mean) grain density, and d is the (mean) grain diameter. Such models aim to find a critical σ_c such that $\sigma > \sigma_c$ guarantees either incipient/cross-bed motion or ejection/resuspension of sediment [7].

This approach requires knowledge of the stress at the boundary. For field-scale studies, this often requires the use of empirical stress laws. Fortunately, when using a DNS, an analytic equation of stress can be used. According to Kundu and Cohen [26], the internal stress tensor of a Newtonian fluid under the Boussinesq approximation is given by

$$\tau_{ij} = -p\delta_{ij} + 2\rho_0\nu S_{ij},$$

where i and j are indices of the spatial coordinates, δ_{ij} is the Kroenecker delta, and

$$S_{ij} = \frac{1}{2}\left(u_{i,j} + u_{j,i}\right) = \frac{1}{2}\left(\frac{\partial u_i}{\partial x_j} + \frac{\partial u_j}{\partial x_i}\right),$$

is the symmetric strain tensor. Using the coordinate system of the experimental domain, and the Einstein summation convention, Cauchy's first law states that the force on a unit area due to internal stress is

$$F_i = \tau_{ij} n_j,$$

where n_j is the outward unit normal of the unit area.

At the bottom boundary, $n_j = \delta_{zj}$. Additionally, for cross-bed transport, the only relevant components of F_i are in the x and y directions. The no-slip boundary condition then implies that the horizontal components of the force per unit area on the bottom boundary are given by

$$\begin{aligned} F_i &= \delta_{zj}\tau_{ij}, \\ &= \tau_{iz}, \\ &= -p\delta_{iz} + \rho_0 \nu \left(\frac{\partial u_i}{\partial z} + \frac{\partial w}{\partial x_i} \right), \\ &= -p\delta_{iz} + \rho_0 \nu \frac{\partial u_i}{\partial z}. \end{aligned}$$

The components of the stress tensor used to investigate thresholds for cross-bed (i.e., along-slope) transport are thus

$$\tau_{zi} = \rho_0 \nu \frac{\partial u_i}{\partial z} \tag{2.30}$$

where the derivative is evaluated at the bottom, and i is one of the horizontal components[14]. It may seem natural to use τ_{zz} to determine the vertical force, and thus the potential for sediment ejection from the boundary. However,

$$\begin{aligned} F_z &= -p + \rho_0 \nu \frac{\partial w}{\partial z}, \\ &= -p - \rho_0 \nu \left(\frac{\partial u}{\partial x} + \frac{\partial v}{\partial y} \right), \quad \text{[By incompressibility]} \\ &= -p. \end{aligned}$$

The last line follows from the no-slip condition, which demands constant $u = v = 0$ along the bottom boundary. Unfortunately, only the gradient of p, and not p itself, can be deduced from the equations of motion [26]. Consequently, this force component and its corresponding stress component(s), are of little practical use. As a result, a false stress

[14]Note that the indices in 2.30 are switched. This is due to a stylistic preference, and it is valid because τ_{ij} is symmetric.

referred to as the 'ejection stress' has been adopted by experimentalists [1, 2, 41]. As discussed by Boegman and Stastna [7], and van Rijn [41], the ejection stress used to investigate thresholds for sediment resuspension is

$$\tau_{ISW} = \rho_0 \tilde{w}^2, \tag{2.31}$$

where

$$\tilde{w}(x,y) = \sqrt{\max_{0 \le z \le \delta} w^2(x,y,z)},$$

and δ is the boundary layer thickness estimate given by Equation 2.26. Note that $\tilde{w}$ could instead be the root–mean–square evaluated over the same z interval [1, 41]. This stress roughly characterizes the vertical kinetic energy injected into the BBL by the flow from the overlying water column. Regardless, both τ_{zi} and τ_{ISW} can be used to empirically determine a threshold σ_c at which the desired type of sediment motion takes place. σ_c is determined for a range of Re, and the resultant curve plotted on σ-Re axes is known as a 'Shields diagram,' which characterizes the Shields model [28].

Two factors prevent an implementation of a Shields model analysis in this investigation. First, as will be discussed in Chapter 3, two events lead to the instigation of transverse motion during the shoaling process. Thus, the assumption of parallel channel flow is violated, and the Shields model with $\tau_b = \tau_{zx}$ loses applicability. However, the Shields model concerned solely with resuspension, where $\tau_b = \tau_{ISW}$, can still be used. This leads to the second issue. Given that Equations 2.11–2.13 contain no sediment model, and that ρ_s and d in Equation 2.29 are thus unspecified, it is impossible to evaluate or even estimate a Shields model using the experiments in the present investigation. That notwithstanding, measuring these stresses gives an approximate idea of the potential for the simulated flows to transport and resuspend sediment at a given stage of the shoaling process, and draws attention to systems that should be reexamined using sediment–coupled models.

Case	H (cm)	c_0 (cm/s)	δ (mm)	Re_{ISW} (-)	Ir (-)	ν ($m^2 \cdot s^{-1}$)	κ ($m^2 \cdot s^{-1}$)	$\tan\theta$ (-)
Large	20.0	11.44	4.18	11440	0.0586	$2.00 \cdot 10^{-6}$	$2.00 \cdot 10^{-6}$	0.052
Medium	15.0	11.44	4.18	8578	0.0677	$2.00 \cdot 10^{-6}$	$2.00 \cdot 10^{-6}$	0.052
Small	10.0	11.44	4.18	5718	0.0829	$2.00 \cdot 10^{-6}$	$2.00 \cdot 10^{-6}$	0.052

Table 2.2: The table of cases. Note that the Schmidt number, $Sc = \nu/\kappa = 1$, for all cases.

2.4 Detecting Vortices

Vortices are coherent structures characterized by correlated circulations about a common centre [22, 24, 25]. A classic topic in vortex dynamics is the interaction between point vortices; this interaction can be analytically modelled using the Biot-Savart law [6]. This can be extended to studying the interaction between tangles of infinitely long vortex filaments. Such an approach can be used to approximate homogeneous, isotropic turbulence at inertial and dissipative scales [13, 29], but it does not have applications beyond the idealized or microscopic realms–let alone to a more complicated system such as a forced, stratified fluid.

Shoaling waves have the potential to generate turbulence in the water column above and below the wave. Characteristic of such flows are chaotic and intertwined vortices (coherent structures characterized by correlated circulations about a common centre) that transport kinetic energy from inertial large-scale features of the flow to small-scale features where viscous dissipation dominates and converts the kinetic energy into heat. Intermediate scale features inertially transfer kinetic energy between each other via vortices stretching vortices of smaller (yet similar) size. Such intermediate interactions are formalized by triad interactions in Fourier space [45], or by structure functions in physical space [13]. This entire process is known as the energy cascade. The same vortices that drive this cascade also boost the irreversible mixing of thermal and chemical energy. As such, the dynamics of vortices has been a major focus in fluid physics.

The application of vortex methods to realistic systems, such as a shoaling wave system, requires a sophisticated model of vortices and their interactions. Advances in computing and measurements allow for detailed data sets that demand high-powered analytical tools alongside a rigorous definition for a coherent vortex. Since the 1980s, several methods for

identifying coherent vortices have been proposed, with the aforementioned applications in mind [13, 25, 24, 15, 11]. Not all methods use physically robust definitions, and several methods correspond to conditions that are just special cases of those used by other methods. As a slightly contrived example of a non-robust method, one definition states that a coherent vortex is region with tightly coiled, circular streamlines; however, in a different inertial frame the coils could become elliptical, and thus this region would no longer be considered a vortex [25, 24]. As an example of an overly-broad definition, a coherent vortex could be a region with a large bulk vorticity; however, layers in a sufficiently strong parallel shear flow would also satisfy this definition.

The definition of a vortex utilized in this thesis is Galilean invariant (so that it works in all inertial frames), and it encapsulates and generalizes the intuitive features of physical vortices that inspired less-robust definitions [25]. That being said, it is only applicable in three-dimensions, and is therefore unsuitable for some vortices that appear in large-scale atmospheric and oceanographic dynamics that are dominated by the rotation of the Earth; issues would also arise when applying this definition to effectively two-dimensional films, such as the surface of a soap bubble. Before stating this definition, however, a few primary quantities must be introduced.

Let the velocity field be represented by u_i, where i is an index over an orthogonal basis for the domain. Using tensor notation, the gradient of the velocity field is $u_{i,j}$. Next, $u_{i,j}$ can be decomposed as

$$u_{i,j} = S_{ij} + \Omega_{ij},$$

where S_{ij} is the symmetric rate of strain tensor, and Ω_{ij} is the anti-symmetric rotation tensor [26]. Consider the eigenvalues of the tensor

$$S_{ik}S_{kj} + \Omega_{ik}\Omega_{kj},$$

which are ordered by decreasing value: λ_m $(m = 1, 2, 3)$. A vortex is then defined as a region of the fluid where the second-largest eigenvalue satisfies $\lambda_2 < 0$ [24]. In practice, visualizing vortices usually requires finding a small number $\epsilon > 0$ and setting $\lambda_2 < \epsilon$. This is known as a thresholding problem, and is discussed in detail by Antonia [3], and more recently by Dubief and Delcayre [15].

This definition has a heuristic physical interpretation. First, note that (excluding some large-scale atmospheric flows, and two-dimensional flows) the pressure inside a vortex is lower than the pressure of its surroundings. While the pressure minimum criterion was once widely used to detect and define vortices, Jeong and Hussain [24] noticed that: i) time-varying strain can create a pressure minimum without any circulation, and ii) viscosity can

erase a pressure gradient within a localized circulation. These observations directly follow from

$$\frac{DS_{ij}}{Dt} - \nu S_{ij,kk} + S_{ik}S_{kj} + \Omega_{ik}\Omega_{kj} = -p_{,ij}$$

which can be derived from the momentum equation (in the absence of body forces) [24]. A generalization of the pressure minimum condition follows by wilfully ignoring the time derivative and the viscous stress term in the above equation. When ignoring body forces, time dependency, and viscosity, the momentum equation (Equation 2.11) implies that $p_{,i} = 0$. Thus, if $S_{i,k}S_{k,j} + \Omega_{i,k}\Omega_{k,j}$ has two negative eigenvalues within a connected region, and because the RHS is the Hessian of pressure, the multi-variable second derivative test implies a pressure at a minimum within that region. Furthermore, λ_2 is defined as the second-largest eigenvalue of this tensor, so $\lambda_2 < 0$ therefore implies that $S_{ik}S_{kj} + \Omega_{ik}\Omega_{kj}$ has two negative eigenvalues [24]. Thus, the intuitive notion of a pressure minimum within a vortex is just a special case of $\lambda_2 < 0$ when the flow is steady and weakly viscous. For an example of a λ_2–vortex field (i.e., a collection of regions where $\lambda_2 < 0$) refer to Figure 2.2. Here an arbitrary data set is used to demonstrate the λ_2–vortex concept, and it is not used anywhere else in this thesis. The temperature data visualized is borrowed with permission from Hanson et. al. [18], but the three-dimensional figures are original. Notice that the vortex rolls in panel b) correspond to overturning regions in the temperature field in panel a).

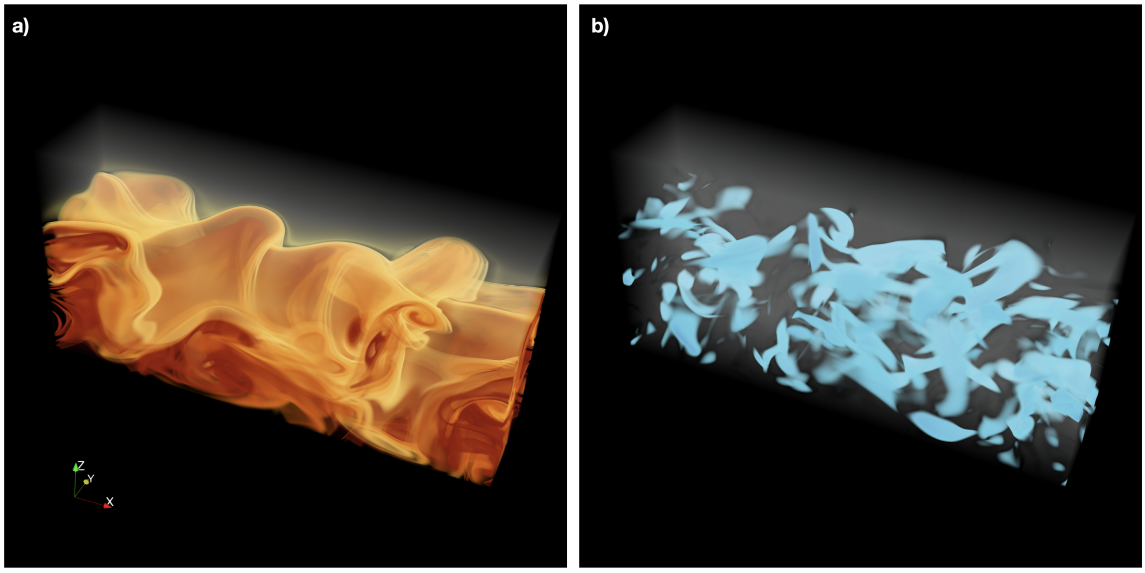

Figure 2.2: A visual demonstration of the λ_2–vortex concept. Panel a) is a temperature field taken from a data set unrelated to the experimental cases discussed in this thesis. Panel b) depicts regions of the fluid where $\lambda_2 < -0.0002$.

2.5 Summary

This Chapter began with an outline of a derivation for the NS equations, which are used to simulate the fluid systems. Next, it discussed details of how these equations are solved, including: the boundary and initial conditions (which are needed to specify a linear–slope system), an overview of the numerical algorithms employed by SPINS, and a discussion of the numerical grid (which established that the simulations performed for this thesis are DNS).

The latter half of the chapter was dedicated to discussing, and defining or deriving the various parameters and quantities that will be used to analyze the simulations. Each wave–slope system is characterized by the wave slope, $S_w = \sqrt{H/L_w}$ and the bed slope, $s = \tan\theta$; these quantities are then combined into $Ir = s/S_w$, which have been used to categorize the types of shoaling dynamics seen in other studies of linear–slope systems [2, 33]. This parameter was therefore used to inform the design of the experiments; namely, it shows that the wave-slope systems studied in this thesis are in the Fission regime. The quantities used to analyze the BBL–wave interaction are: the bed stresses, τ_{zx} and τ_{zy}; the ejection pseudo-stress, τ_{ISW}, which can be used as an estimate for the potential of a

wave to induce sediment resuspension; and, λ_2, a quantity that satisfies $\lambda_2 < 0$ in regions occupied by three-dimensional coherent vortices. These vortices are visual tools, and can be used to qualitatively assess the mixing and sediment transport potential of a given wave.

The results of the simulations described in Table 2.2 can now be analyzed with the aid of these quantities and with these fundamental concepts in mind.

Chapter 3

Results of the Simulations

A shoaling wave of depression transforms as it interacts with the slope. The BBL beneath the wave also transforms, and eventually the evolution of the BBL becomes an essential component of the evolution of the wave. The transformation of the wave can be organized into the following stages: i) incidence upon the slope, ii) fission along the slope, and iii) bolus formation and degeneration near the intersection of the slope and the pycnocline [46]. For a visual example, refer to Figure 3.1, which depicts the evolution of the density field of the Medium case. In Figure 3.1, the first stage corresponds to the transition from panels a) to b), the second corresponds to the transition from b) to c), and the third corresponds to the transition from c) to d). Of particular importance is the transition from c) to d), during which BBL instabilities (if present) overturn the pycnocline and cause wave breakdown (note the mixed pycnocline near $x = 3.75$m in panel b) of Figure 3.2).

In each experimental case, these stages were observed to correspond, respectively, to the following qualitatively distinct BBL instabilities: i) a *prograde*[1] jet, ii) a separation bubble, and iii) lobe-cleft instabilities and shear-instabilities. This chapter is organized by the stages and their instabilities: the first section begins by discussing the initial ISW-D, and the the prograde jet; the second reports on the formation of separation bubbles, and secondary vortex instabilities; the third section discusses the destruction of the wave by way of bolus formation, and the concurrent generation of lobe-cleft and shear instabilities; finally, the fourth section summarizes the narrative of the chapter.

Every section presents data from at least two of the three cases simultaneously; this is done i) to highlight the broad similarities of the stages described above, and ii) to use

[1] i.e., along the positive streamwise direction; likewise, *retrograde* indicates something that is against the positive streamwise direction.

the broad similarities to accentuate the differences in the manifestation of the BBL-wave interactions caused by varying the amplitude of the wave. To spoil the punchline, the Large case shows extremely violent overturning of the pycnocline due to vortices generated by the wave-BBL interaction; the amplitude is then reduced by half (the Small case) and the vortices are no longer present, and no overturning occurs; the Medium case has, as its name suggests, an intermediate amplitude, and weaker vortices are present, and they also overturn the pycnocline (though, as expected, with less violent results than the Large case). As will be seen in the subsequent sections, the other instabilities also exhibit similarities and differences when the wave amplitude is varied. Throughout, results from these experiments will be compared with results from other numerical investigations (such as Arthur and Fringer [4], Olsthoorn and Stastna, [34], and Xu et. al. [46]), and with results from physical experiments (such as Ghassemi et. al. [17], Moore et. al. [32], and [43]).

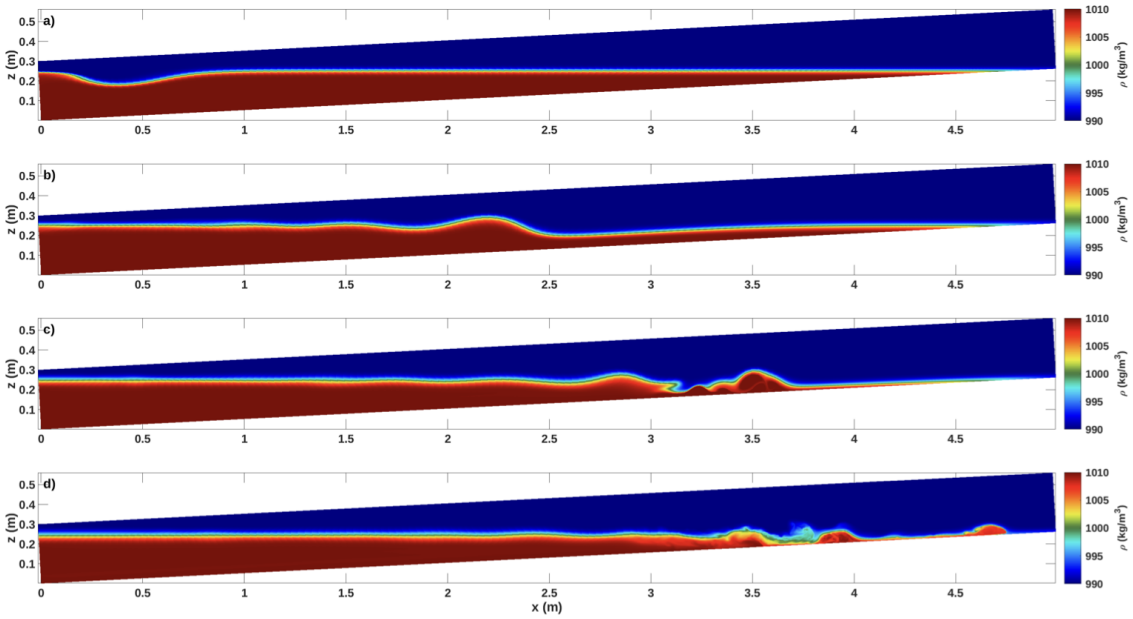

Figure 3.1: Evolution of the density field from the Medium case. Each panel contains a vertical cross-section of the density field at $y = 0.128$m at a given time. a) shows the wave during the prograde jet phase ($t = 4$s), b) shows the wave fissioning during the separation bubble phase ($t = 29$s), c) shows the breakdown of the wave when the lead separation bubble bursts ($t = 45$s), and d) depicts the bolus phase ($t = 61$s).

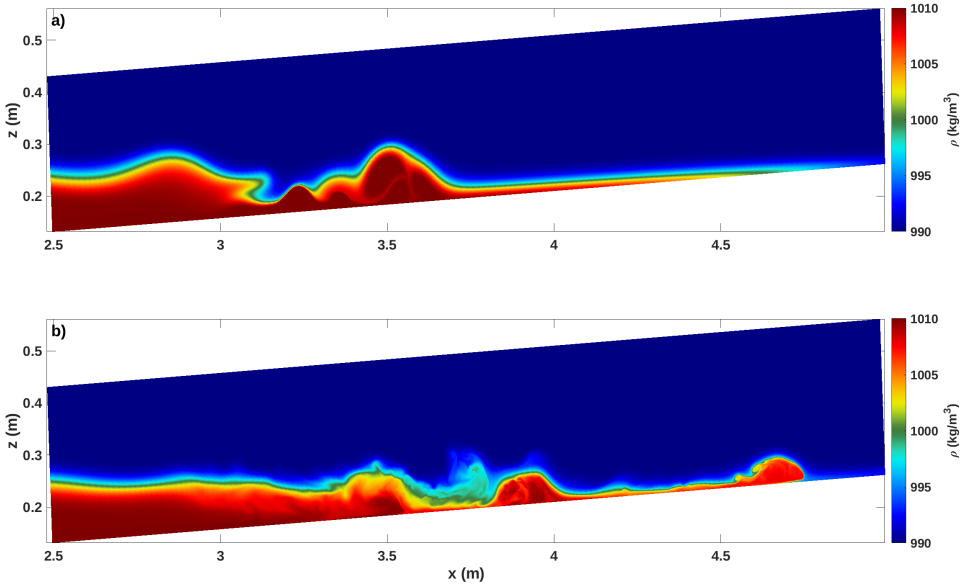

Figure 3.2: Formation of a bolus during the transition from the fission phase to the bolus phase in the Medium case. Each panel contains a vertical cross-section of the density field at $y = 0.128$m at a given time. The wave degenerates into three boluses. a) is the density field at $t = 45$s, and b) is the density field at $t = 61$s.

3.1 The Prograde Jet Phase

ISWs fission from the initial disturbance of the pycnocline, which is larger in amplitude than the ISW amplitude. The amplitude of the emerging ISWs increases with the amplitude of the disturbance. All waves in the numerical experiments translate with nearly the same speed; only the Large case leads to localized overturning during the adjustment phase of evolution. This instability is not depicted, because it does not ultimately impact the interaction between the wave and the BBL. What will impact the interaction, however, are the streamwise and vertical currents induced by the wave, which are very much dependent on the initial amplitude.

In all cases, the shoaling wave of depression induces a prograde jet in the BBL within three seconds of the lock release. Figure 3.3 shows the streamwise velocity field of each case at the end of the strictly 2D portion of the evolution. The jet is the band of rightward current in the BBL (the orange-red streak at the bottom of each tank). The magnitude of the jet's velocity increases as the wave shoals. The magnitude of, and the rate of, the intensification of the jet increases with the initial amplitude of the wave; this can be seen in Figure 3.3, as the horizontal flow induced by the jet in the Small case (panel c)) is an order of magnitude weaker than the other cases.

At the stage depicted in Figure 3.3, the leading wave of elevation has already passed the turning point, and the ISW-D is beginning to fission into a wave-train. The front portion of each jet is under the leading wave of elevation, and they are each contracting into the separation bubble typical of ISW-Es. For an example, of this process refer to Figure 3.4, which depicts panel a) from Figure 3.3 after 2s have passed, and with a window[2] that better shows the disparity in height between the separation bubble and the jet. After pinching, the back of the jet will remain where it is, and it will be modulated by the newly formed trailing waves; in the Large case, the eventual result is the presence of noticeable undulations in the u field in the boundary layer near the turning point between $t = 64$s and $t = 68$s. As will be discussed in greater detail in Section 3.4 and in Chapter 4, these undulations might suggest a mechanism for formation of the sandwaves observed by Ma [30]. However, as will also be discussed, the relative weakness of the current in the jet to the wave-induced currents and to the current in the separation bubble, raises doubts about this interpretation.

The rate of formation of a bubble increases with the amplitude of the initial wave. This is sensible, as the amplitude of the wave determines the strength of the currents, and the separation bubble instabilities would not form without the adverse shear current formed

[2]This window is both wider and shorter than that in Figure 3.3.

by the remnants of the initial ISW-D [7, 9, 10, 14, 46]. The next section discusses the evolution of these separation bubbles.

One order of business needs to be addressed before proceeding, and that is to describe a type of figure that will be used repeatedly throughout this thesis. Consider Figure 3.5: this is a 'total evolution diagram' (henceforth TED). It depicts: in panel a), the density field at a given time; in panel b), the streamwise velocity at a given time; in panel c), the transverse velocity field at a given time; in panel d), the ejection stress at a given time; and, in panel e), time series of the root-mean-square of each of the bed stresses, where the mean used is the domain average. Note that in panel e) a vertical grey line highlights the time under consideration. These diagrams succinctly capture the essential information of the system at a given moment (in panels a)-d)), and contextualize this information within in the total evolution (using panel e)). Note that panels a)-c) are vertical cross-sections at $y = 0.128$m while panel d) is a necessarily horizontal view of the bed (psuedo-)stress, τ_{ISW}. As an aside, to keep the subject in the frame, the frame must translate with a speed close to the speed of each wave; in each case, this is approximately 68.75% of the long wave speed in deep water, c_0, and it is calculated as discussed in Subsection 2.3.1.

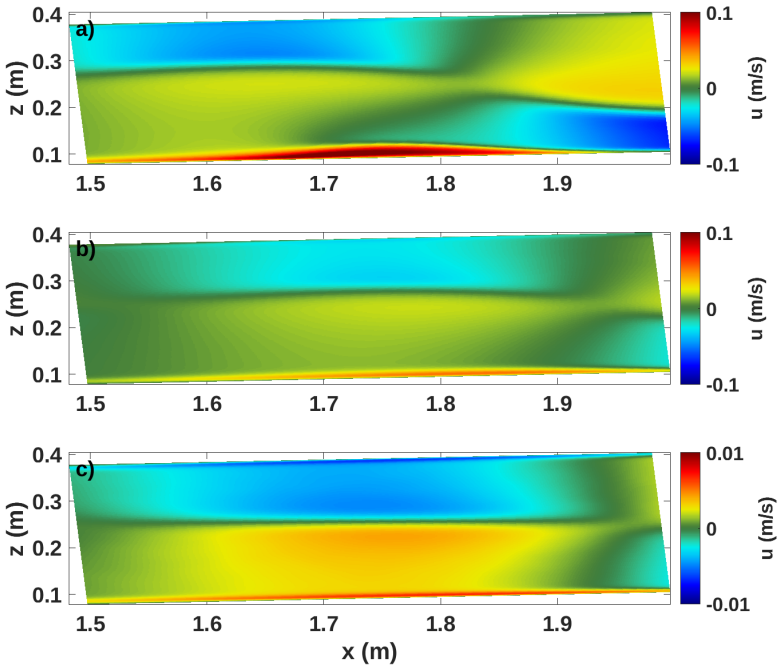

Figure 3.3: The cross-section of the streamwise velocity field at $y = 0.128$m, and $t = 24$s for each case. a) is the Large case, b) is the Medium case, and c) is the Small case.

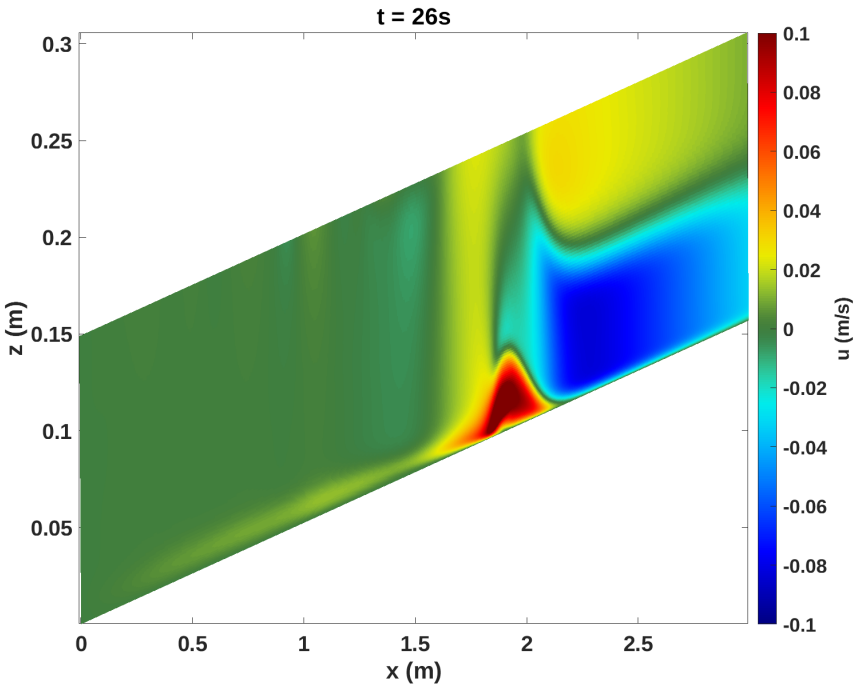

Figure 3.4: The cross-section of the streamwise velocity field at $y = 0.128$m, and $t = 26$s for the Large case.

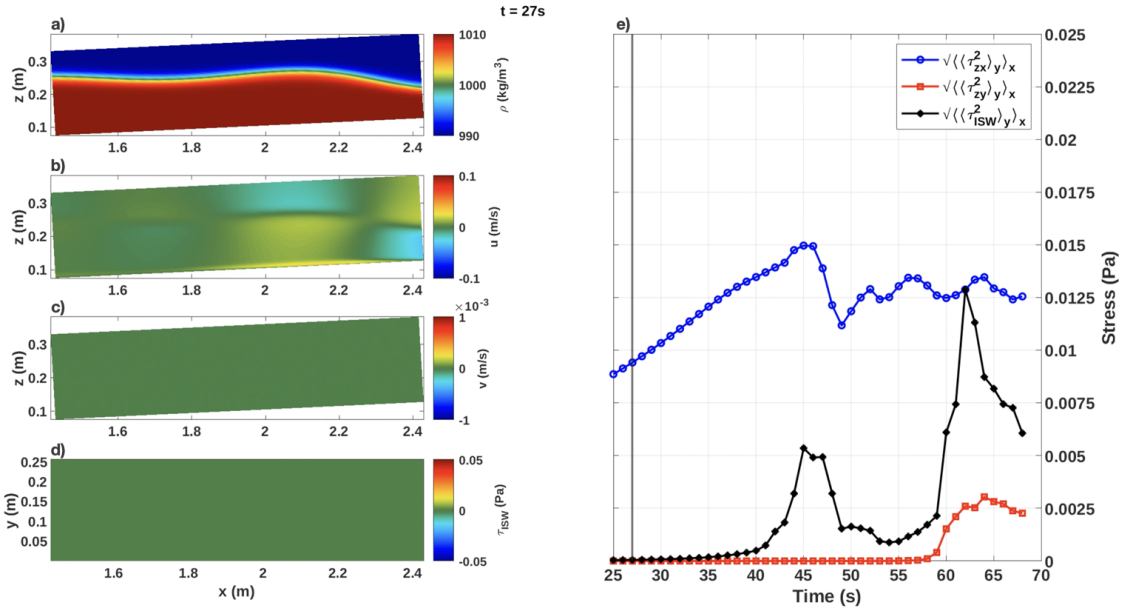

Figure 3.5: Total evolution diagram of the Small case at $t = 27$s.

3.2 The Separation Bubble Phase

3.2.1 Formation of the Separation Bubble

The separation bubble at the front of each jet continues to contract during the fission process. The bubbles initially sit near the front of the wave of elevation, as they have been depicted [7]. As a bubble contracts, a band of ejection stress forms to the right of the bubble, and then a stronger band of ejection stress forms to the left; an example of these can be seen in the TED, Figure 3.6d) for the Small case (note that they are present in all cases). As usual, a strong upwards current sits at the front half of the leading wave of elevation; what is interesting, though, is that a sheet of vertical momentum branches off of this current, and penetrates the boundary layer at the same location as the left band of ejection stress. An example of this sheet can be seen in Figure 3.7, which is a depiction of a horizontal cross-section at $y = 0.128$m of the vertical velocity field from the Medium case. In this figure, two black arrows denote the location of the aforementioned bands of stress. As can be seen in the figure, the contact point of the momentum sheet, highlighted by the left black arrow, coincides with the left band of stress, as mentioned. Likewise, the right band of ejection stress coincides with the contact point of the aforementioned strong vertical current and the BBL, and this contact point is highlighted by the right black arrow in Figure 3.7. The shape of the bands in Figure 3.6d), and the lack of a transverse current in panel c) both indicate that the formation of a separation bubble is a two-dimensional process. Additionally, no other case provides evidence of a transverse current or of spanwise variation in any field during the formation of the initial separation bubble.

Once the bubbles are approximately $35-40$cm in width and $3-4$cm in height, they begin to induce smaller separation bubbles within themselves. Figure 3.8 depicts the bubbles at this stage, via a vertical cross section ($y = 0.128$m) of the streamwise velocity field, for each case. The streamwise currents of the internal separation bubbles are oriented opposite to those of the parent bubbles, which are themselves oriented with the positive streamwise direction; i.e., the parent bubbles have prograde currents, so the internal bubbles have retrograde currents. When the internal bubbles begin to form, the previously discussed band of ejection stress on the left of the bubble splits into two separate bands; the leftmost band still bounds the parent bubble, and the inner band sits to the left of the internal bubble. Two weaker bands also appear, and can be seen in the TED in Figure 3.9d); the weak bands are the right boundaries of the separation bubbles. This can also be seen in the other cases, though the bounding bands are stronger and weaker in the Large and Small cases, respectively. The perfectly rectangular bands of ejection stress, the transverse

current being weaker than $O(10^{-4})$m/s, and the maximum spanwise standard deviation of the streamwise velocity field being weaker than $O(10^{-4})$m/s, across all cases, all suggest that the formation of an internal separation bubble is a predominately two-dimensional process, with weak three dimensional growth.

During the shoaling process, the leading wave of elevation in the Medium and Small cases produces three internal separation bubbles, while in the Large case it only produces two. The larger–amplitude cases produced larger internal separation bubbles with stronger retrograde currents; it is only these larger and stronger bubbles that precede secondary and higher instabilities[3] capable of generating significant spanwise variation. Indeed, the fields of the Small case remain two-dimensional until the bolus phase, and it is only the larger amplitude cases that produce coherent vortices and significant transverse currents during the fission phase. The production and evolution of these vortices are discussed next.

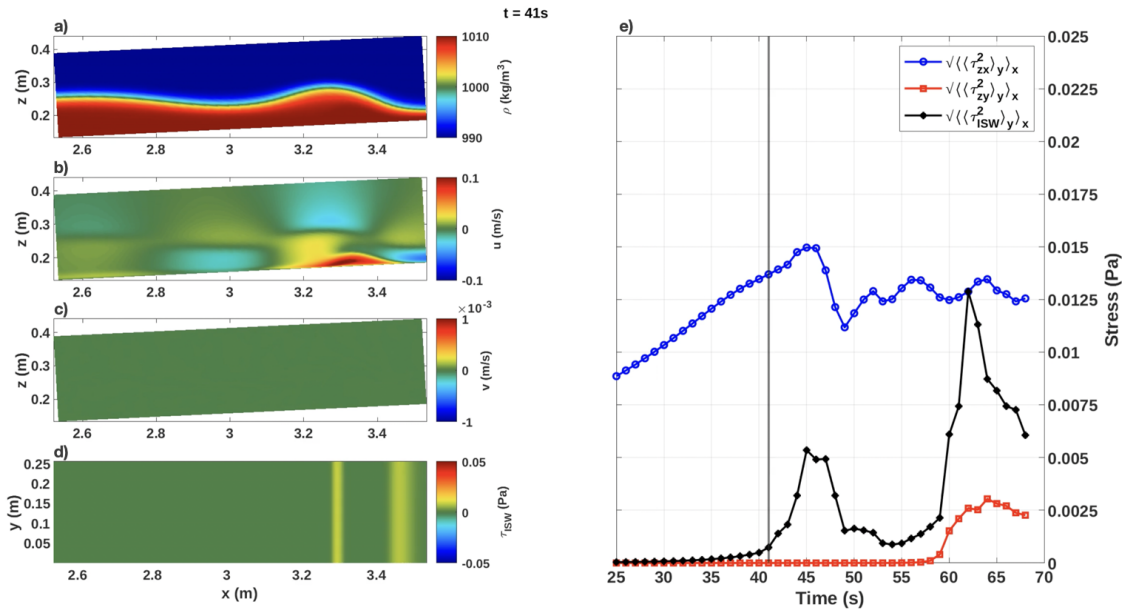

Figure 3.6: Total evolution diagram of the Small case at $t = 41$s.

[3] i.e., only their bubbles 'burst'–a term to be explained in great detail in the next section

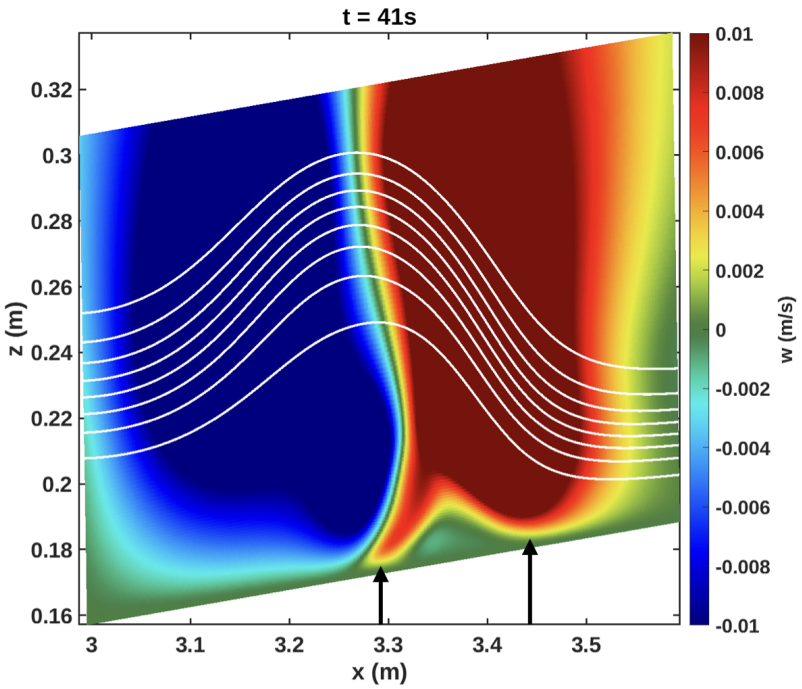

Figure 3.7: The cross-section of the vertical velocity field at $y = 0.128$m, with superimposed density contours for the Small case at $t = 41$s. The contours are evenly spaced between 992.2kg/m^3 and 100.8kg/m^3. The black arrows highlight the location of the stress bands from Figure 3.6d).

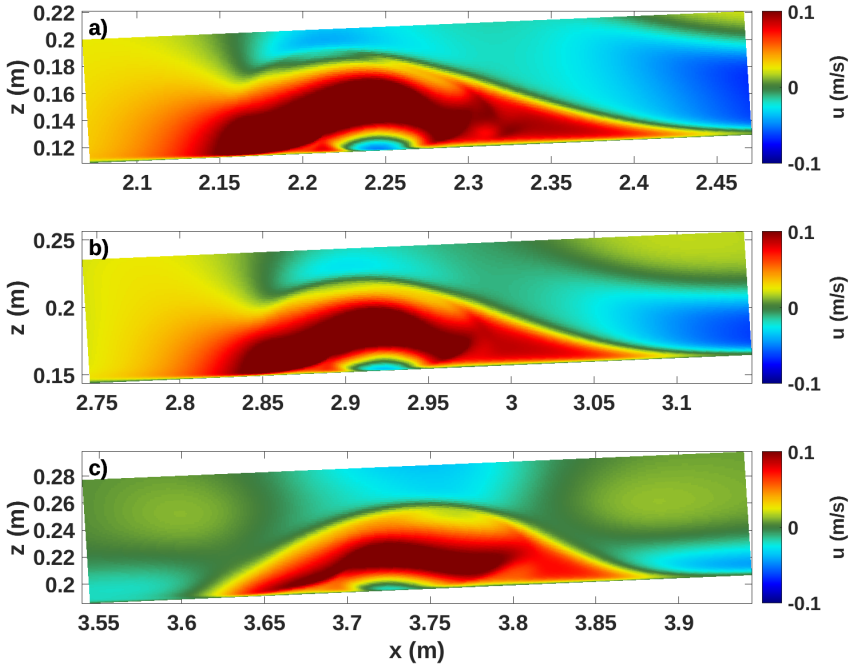

Figure 3.8: The cross-section of the streamwise velocity field at $y = 0.128$m for each case. a) is the Large case at $t = 30$s, b) is the Medium case at $t = 37$s, and c) is the Small case at $t = 47$s.

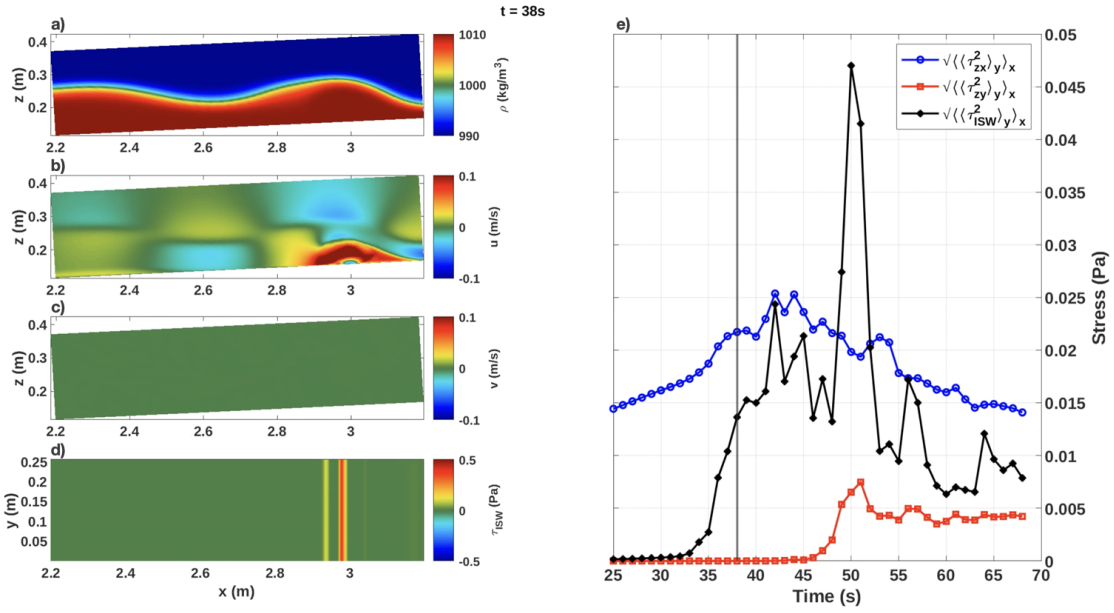

Figure 3.9: Total evolution diagram of the Medium case at $t = 38$s.

3.2.2 Bursting

An internal separation bubble unsteady region will move towards the back of the parent bubble and the leading ISW-E. In the Small case, each internal separation bubble degenerates before it reaches the back of the parent bubble; in the other cases, at least one internal separation bubble exits the parent bubble. When it does so, a portion of the parent bubble will exit with it, and they have the potential to form a vortex. This latter process is known as 'bursting' [46]. Consider the Large case first: in the transition between panel a) in Figure 3.8 (from the previous subsection) and panel b) in the TED in Figure 3.10, the parent bubble is split by the internal bubble; the left portion of the parent travels with the internal bubble up and to the left, away from the boundary layer. These adjacent regions of opposite current constitute a vortex, which may experience transverse instability; they are highlighted by a black square in panel b) of Figure 3.10. Indeed, the nascent transverse currents of this instability can be seen in Figure 3.10c). This vortex intensifies, and draws down the pycnocline that sits to its immediate left. As it does this overturns the pycnocline, and subsequently generates a baroclinic vortex of the opposite polarity; this vortex is generated by a portion of the retrograde current that was above the parent bubble, but that was entrained during the burst. The opposing currents that will go on to create the baroclinic vortex are highlighted by a white square in panel b) of Figure 3.10. The overturning of the pycnocline generates strong density gradients in the lower to middle water column. The result of this overturning can be seen to the left of $x = 2.5$m in panels a)-d) of Figure 3.11 (a TED). While the vortex produced by the first internal separation bubble does this, a second internal bubble forms, which can be seen around $x = 2.6$m in Figure 3.10b). The bands of ejection stress about the second internal bubble, seen in panel d), show spanwise variation; accordingly, the structure that emerges appears less like a vortex than it does a burst of coherent motion growing out of the BBL. The effects of this burst can be seen near $x = 3$m in panels a)-d) of Figure 3.11.

The scale and span of the coherent vortices generated can be appreciated by considering the λ_2 vortex field in Figures 3.12 in and 3.13. These figures each contain false-colourings of volumes where $\lambda_2 <= 0.0002$, though the latter figure also superimposes a volume of the density field that conatains the pycnocline. The complex patterns in panel d) of Figure 3.11 overlap with the regions where the vortex field in Figure 3.12 touches the bottom boundary. The large magenta vortices in the middle, which are the vortices formed by the first separation bubble, produce the most ejection stress at this time ($t = 39$s). Meanwhile, the green-grey-magenta cloud of vortices to the left stirs and mixes the pycnocline and even induces spanwise structure in the pycnocline as it does so (see Figure 3.13). The smaller cloud of vortices to the right corresponds to the burst from the second internal separation

bubble; these vortices do not interact strongly with the pycnocline, but they do create ejection stress in the bottom boundary layer. They also become trapped under the leading wave of elevation. As the instabilities from the burst grow they begin to take the form of a vortex, but, as can be seen in Figure 3.12, the region beneath the leading wave of elevation rapidly becomes turbulent and the coherent structure disintegrates. The strong turbulent spanwise motion also disrupts the formation of the third separation bubble that is observed in the other cases. In Figure 3.11 it is clear that this whole process creates a spike in all the bed stresses, between $t = 37$s and $t = 52s$; the trailing waves are much weaker, and do not produce such intense structures, as is evidenced by the dip in the ejection stress when the leading wave of elevation enters the bolus phase and its internal turbulent currents begin to dissipate.

This process is similar, if less bombastic, for the Medium case. The first internal separation bubble exits the parent bubble, and takes a portion with it. In this case, however, this region does not travel upwards at all; additionally, the entrained portion is not completely detached from the parent bubble, as can be seen in Figure 3.14b) above $x = 3.3$m. The opposing currents once again constitute a vortex which i) energizes weak transverse currents, and ii) overturns the pycnocline above $x = 3.1$m in panel a). During overturning, the vortex merges with the region of strong retrograde current between $x = 3.0$m and $x = 3.2$m; as it does so, it induces weak transverse currents and vortical structures. The weak, baroclinic overturning of the pycnocline once again generates a strong interaction of the pycnocline and boundary layer, and stronger transverse currents than those from the initial vortex produced by the bubble. These effects are most visible in panels a), d) and e) from Figure 3.15. In a) the overturning leads to mixing across the pycnocline between $x = 3.1$m and $x = 3.6$m; in d), the ejection stress between $x = 3.8$m and 4.0m is both intense and exhibits strong spanwise variation; and, in e), there are clear spikes in the ejection stress and in the transverse stress between $t = 49$s and $t = 52$s.

Under the leading wave, another separation bubble is produced; it can be seen in panel b) of both Figure 3.14 (at $x = 3.5$m) and Figure 3.11 (at $x = 3.9$m). Its evolution is similar to the first bubble, but it creates a weaker vortex. However, the vortex still interacts with the pycnocline, which is now closer to the bottom (between $x = 3.4$m to $x = 3.8$m in panel a)). The vortex created by the second bubble also induces transverse currents which overtake and modulate the third bubble in the middle of its growth–showing that three-dimensional growth, though slower, eventually dominates two dimensional growth in these systems. Referring to panel d) of Figure 3.15, the greatest ejection stress is beneath the leading wave. Additionally, there is a large spike in the domain-rms of the ejection stress at this time—the largest value across all cases. Alongside the form of the transverse velocity, this suggests that the chaotic currents induced by the final two bubbles reinforce each other

while they drive the transition to turbulence under the wave. This is in stark contrast to the large amplitude case, where—paradoxically—the strong, turbulent currents from the second bubble prevent the generation of a third bubble, and in turn reduces the maximum domain-rms of the ejection stress.

After bursting, the leading ISW-E begins the bolus phase, and the turbulent currents beneath it begin to dissipate. As stated previously, though, the separation bubble under the leading ISW-E never bursts in the Small case. Consequently, no turbulent currents are present. In this case, the leading ISW-E continues to produce extremely small internal separation bubbles that degenerate rapidly.

Though quite a bit of emphasis has been put into describing the process of bursting, what may not be clear is the significance of the presence bursting and its products. As has been stated repeatedly, bursting leads to vortex formation, which leads to turbulence under the pycnocline and mixing across the pycnocline. Here, for perhaps the first time in three dimensions, there is strong evidence that systems in the fission regime are not just capable of mixing the water column, but they are also capable of doing so violently (as can be seen in the three-dimensional figures, Figures 3.12 and 3.13, and near $x = 2.4$m in Figure 3.11); that is, these waves are likely to be able to resuspend sediment and contribute to nutrient transport throughout the water column. Then, because the shallow slope of the coastal shelf [7] implies that fission-regime waves should be the most abundant waves in this environment, fission–regime waves are likely to play crucial roles in the biogeological cycles in the coastal ocean.

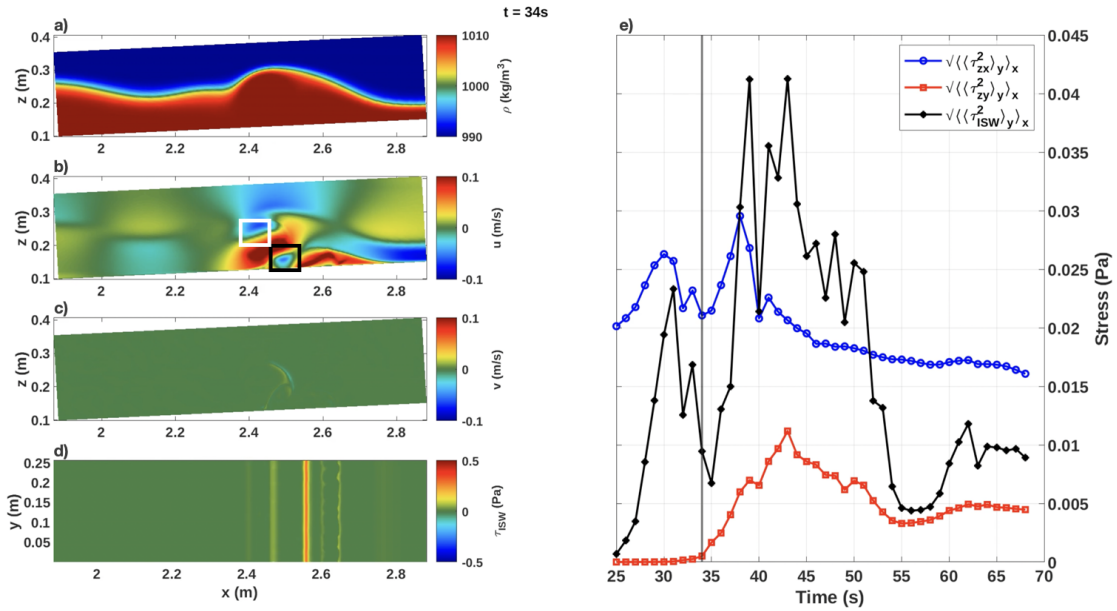

Figure 3.10: Total evolution diagram of the 1A case at $t = 34$s with annotations in panel b). The black square highlights the opposing currents that create the first vortex, and the white square highlights the opposing currents that create the baroclinic vortex that overturns the pycnocline.

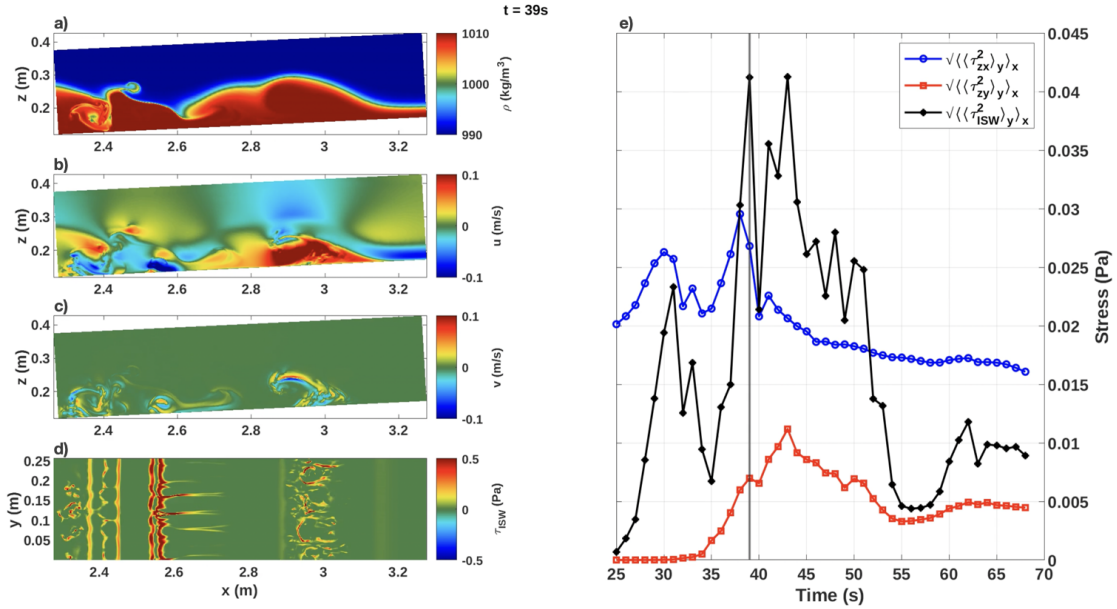

Figure 3.11: Total evolution diagram of the Large case at $t = 39$s.

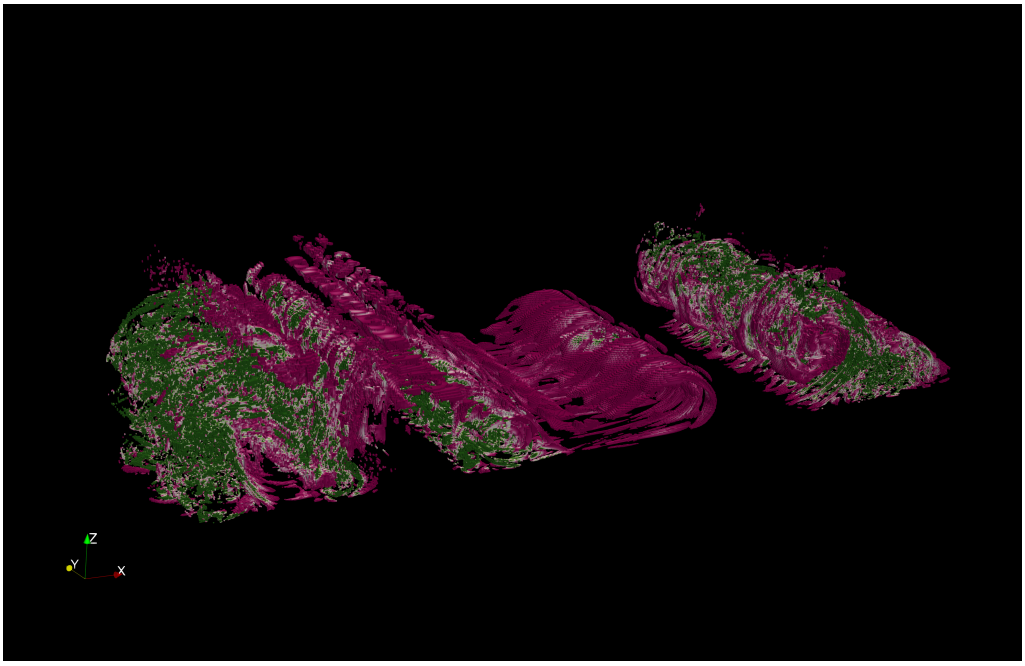

Figure 3.12: Three-dimesnional, volumetric depictions of vortices produced by the burst of the first and second internal separation bubbles at $t = 39$s in the Large case. Volumes with vortices satisfy $\lambda_2 < -0.0002$. Numerically, the colourmap has Magenta regions closer to $\lambda_2 \approx -0.0002$, green regions closer to $\lambda_2 \to -0.1$ (this is a saturation choice, since $\min(\lambda_2) = -512.0$), and white regions as the intermediate colour. Physically, magenta regions can be roughly interpreted as having a weaker degree of three-dimensionalization, and the white and green regions can be roughly interpreted as having a stronger degree of three-dimensionalization.

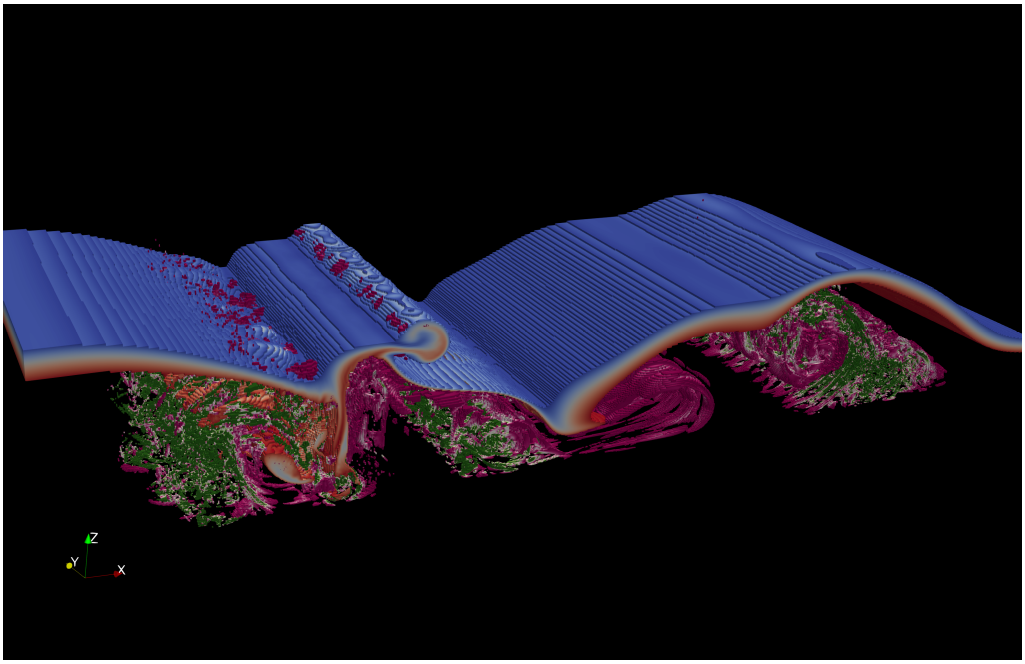

Figure 3.13: Same as the Figure 3.12, but with a three-dimensional, volumetric depiction of density field about the pycnocline superimposed on the vortex field. Red regions are more dense, blue regions are less dense, and grey regions are close to the reference density, ρ_0. Once again, this is for the Large case.

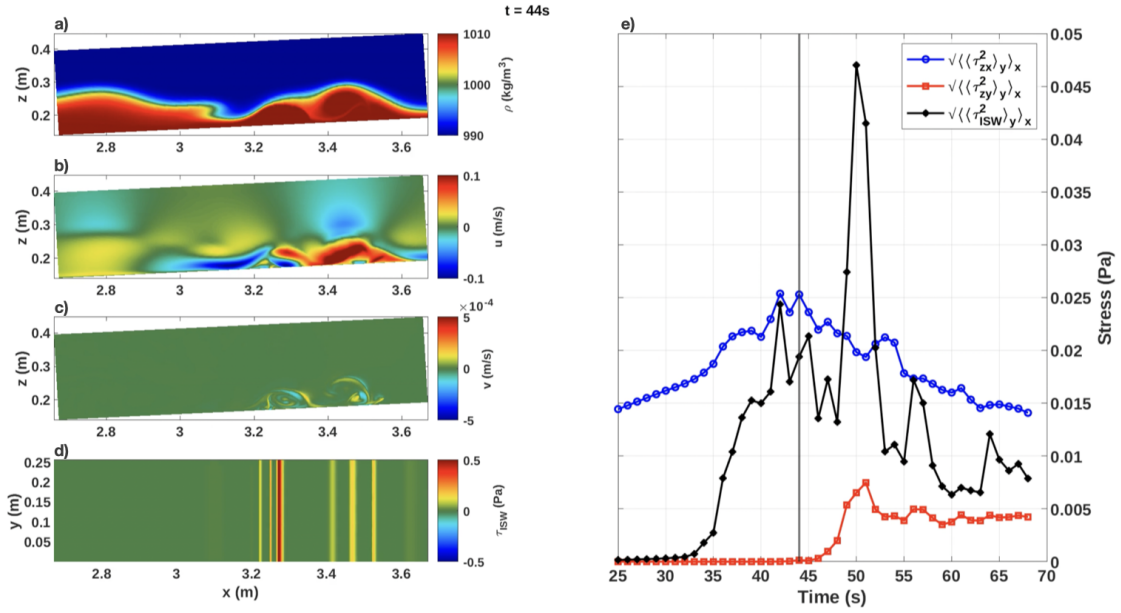

Figure 3.14: Total evolution diagram of the Medium case at $t = 44$s.

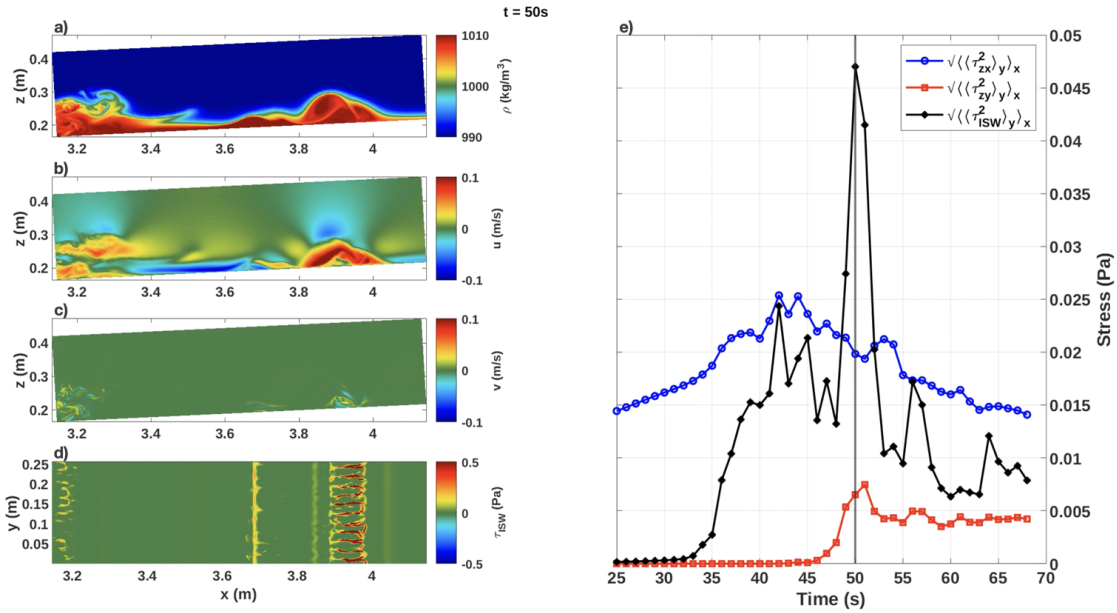

Figure 3.15: Total evolution diagram of the Medium case at $t = 50$s.

3.3 The Bolus Phase

As the wave evolves into a bolus, the parent bubble will come to occupy the entire region beneath the wave. The chaotic currents under the wave from the previous phase begin to dissipate. Consistent with Figure 9a from the experimental work of Ghassemi, et. al. [17], the parent bubble was surrounded by a retrograde current near the bolus birth point. This region does not persist, and, as can be seen in panel b) of Figure 3.16 (a TED), two patches of prograde motion that rest on the 2 o'clock and 10 o'clock positions along the boundary of the bolus are present during the final moments of the shoaling process. In a reference frame moving with the wave, this becomes a region of backflow surrounding the bolus, with peaks in retrograde current at the top, back, and front of the bolus; see Figure 3.17, which depicts, from the Large case, a vertical cross-section ($y = 0.128m$) of the density field, the streamwise velocity field (in a frame moving with the bolus), and the vertical velocity field (in a frame moving with the bolus). Remarkably, this figure aligns with Figure 10 of Wallace and Wilkinson [43] which infers this information from experimental measurements of the relatively thin bolus boundary using technology from 1988.

In every case, as the bolus translates and shrinks, the retrograde current at the front vanishes; an example of this can be seen in the TED, Figure 3.18b). During this time, the bolus begins to act as a gravity current: the front of the bolus separates from the bottom boundary; thus, at the front of the bolus, denser fluid moves over lighter fluid at rest and the combined shear and buoyancy induce lobe-cleft instabilities [19]. At the same time, the bolus leaks dense fluid out of its rear face, which creates regions of circulating currents within the bolus core (see Figure 3.17). This circulating current entrains portions of the density interface that bounds the bolus. Together, the shear across the boundary combined with the aformentioned entrainment produce billows along the top and rear of the bolus. Figure 3.20 depicts these billows from each case via a vertical cross-section of the density field at $y = 0.128$m. They appear as intrusions along the top and rear of the bolus boundary, which are regions of high shear. They do not appear to have the form the iconic Kelvin-Helmholtz billows, as some intrusions do not curl up into themselves (see panels b) and c)). Given that, earlier, the roll-up of the pycnocline by the baroclinic vortices was two–dimensional, it is fair to ask if these billows are also two–dimensional. The answer to that question lies in Figure 3.21, which depicts the lobe-cleft instabilties from each case via a horizontal cross-section of the density field at $z = 4.1$mm. These figures show a great degree of spanwise variation in the front of the bolus near the bottom boundary. However, the next question to ask is whether or not the three-dimensional structure at the front of the bolus reaches the top and back of the bolus (where the billows reside). Before answering that question, quickly note that both of these figures are in excellent agreement

with Figure 8 from Ghassemi, et. al. [17], which shows the same structures in the dyed fluid of their late-stage boluses.

To answer the question of the spread of spanwise variation, refer to Figure 3.22, which depicts the pycnocline about the bolus and the λ_2–vortex field at $t = 60$s in three dimensions. Panel a) depicts the pycnocline about the bolus, and it is evident therein that the spanwise structure of the lobe-cleft instabilities influences the three-dimensionalization of the billows of the shear instabilities. Panel b) of the same figure shows the λ_2–vortex field, and panel c) shows the same superimposed over the pycnocline. In these panels, we see vortex cores emerging from the clefts, and extending towards the back along the bolus boundary; thus, it is the transverse roll-up from the lobe-cleft instabilities that produces spanwise variation along the outer boundary of the bolus, and subsequently inducing spanwise variation in the billows. The interior vortices highlight the turbulent nature of the circulating currents within the bolus.

In the Small case, the processes that arise during bolus degeneration result in the strongest transverse currents and ejection stress yet seen in this case. In fact, it is only during bolus degeneration that this case exhibits any significant three-dimensional structure. This is apparent in panel e) of Figure 3.16 (a TED). On the other hand, while the Large and Medium case both exhibited three-dimensional structure well before bolus degeneration, this process caused an additional increase in quantities that indicate spanwise variation. Panel e) of Figure 3.18, which corresponds to the Large case, shows a slight increase in transverse bed stress after a period of slight decay. This is less obvious in panel e) of Figure 3.19 (a TED), which corresponds to the medium case. Nevertheless the fact remains that the Small case began to three-dimensionalize during bolus formation, and this suggests that the other cases also undergo a second period of three-dimensionalization independent of the burst.

Panel e) of Figure 3.18 shows a greater spike in ejection stress for the Large case at $t = 62$s, after the rapid decay between $t = 50$s and $t = 55$s. This does not indicate transverse motion, but it does show a second period of excitation of the boundary layer. A similar pattern should appear in Figure 3.19, but dynamic interaction between the pycnocline and the currents produced during the bubble phase overshadow what is happening under the bolus in the Medium case. Fortunately, these effects are isolated in the Small case, and from the observations of that case it is clear that during the bolus phase, a second, independent burst of activity manifests as growing transverse currents in the bolus, as lobe-cleft instabilities at the front of the bolus, and as billow instabilities along the top and rear of the bolus.

As the streamwise momentum dissipates once the bolus begins to degenerate, the dense

fluid within will sink down the slope, and the drawback current will interact with the trailing waves and boluses. Ghassemi et. al. [17] state that one wave of depression corresponds to one bolus; however, in the present investigation, the singular initial ISW-D produces three boluses before the end of the simulation—see panel b) in Figure 3.2. The discrepencey between their results and the present results is likely due to their wave generation mechanism, which is a paddle that produces a continuous train of nonlinear waves. This continuous train would obfuscate the contribution of the much weaker trailing waves which emerge during fission, and which produce the multiple boluses per initial wave of depression observed during this investigation.

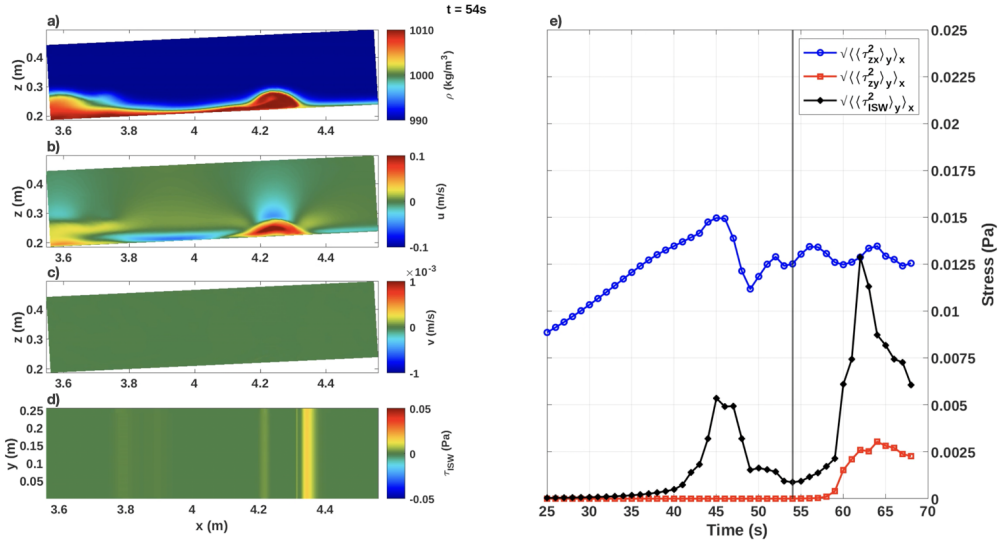

Figure 3.16: Total evolution diagram of the Small case at $t = 54$s.

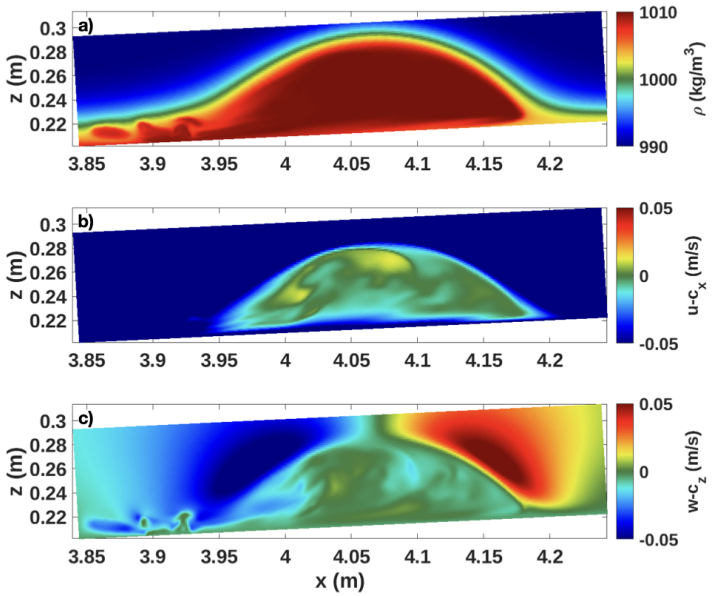

Figure 3.17: The structure and flow of the the Large case leading bolus at $t = 53$s and $y = 0.128$m. Panel a) is the density field, panel b) is the streamwise velocity in the frame of the bolus, and panel c) is the vertical velocity in the frame of the bolus. $c_x = 7.85$cm/s and $c_z = 4.12$mm/s are the components of the wave velocity with total speed $c = 0.6875c_0 = 7.87$cm/s.

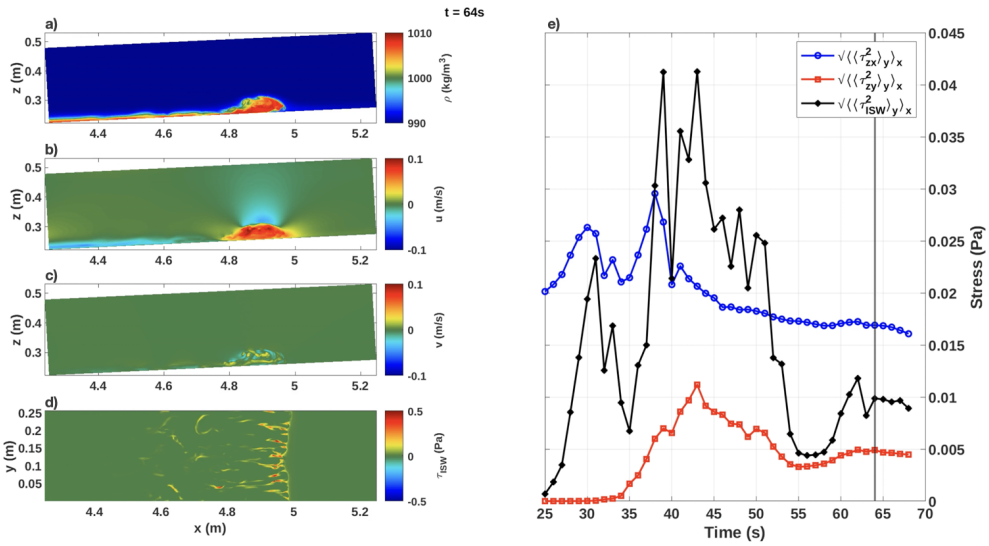

Figure 3.18: Total evolution diagram of the Large case at $t = 64$s.

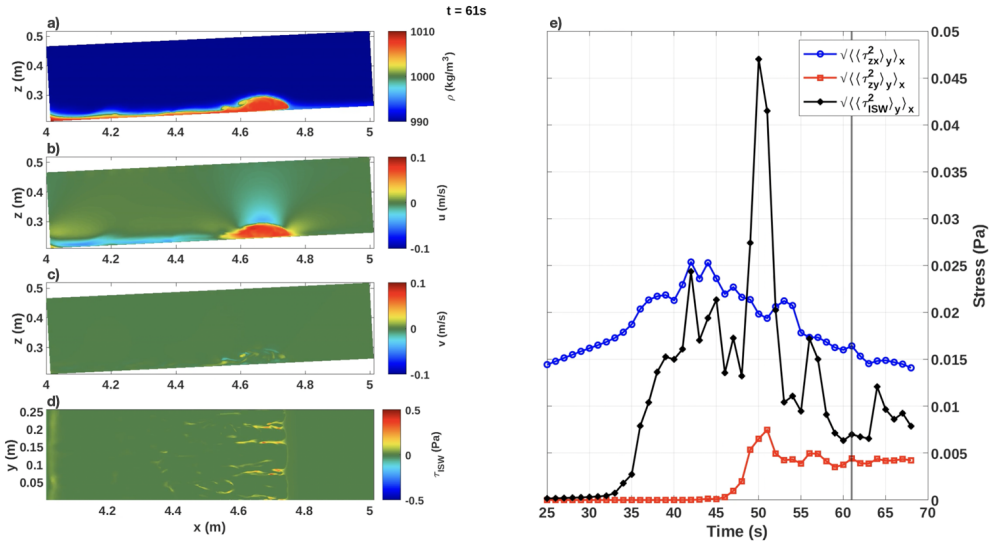

Figure 3.19: Total evolution diagram of the Medium case at $t = 61$s.

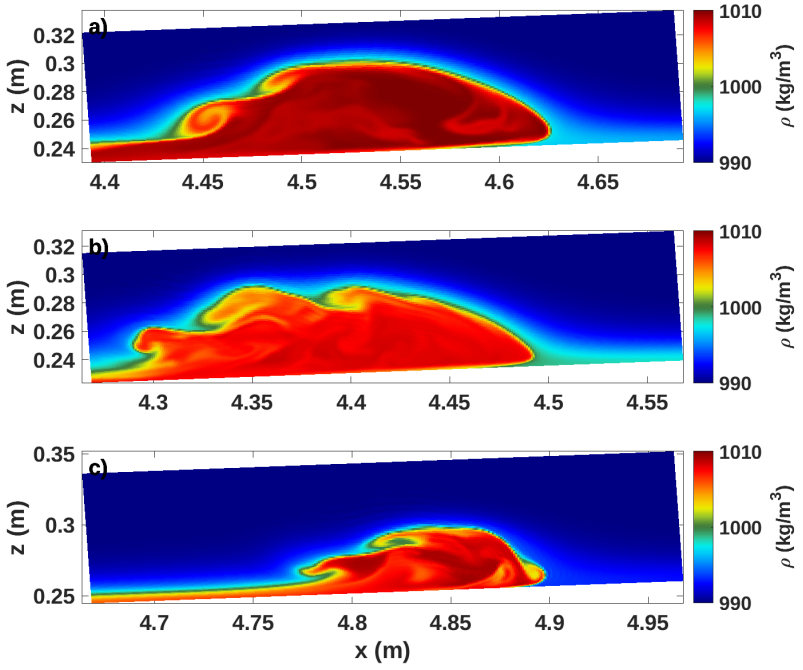

Figure 3.20: The cross-section of the density field at $y = 0.128$m for each case. a) is the Large case at $t = 59$s, b) is the Medium case at $t = 57$s, and c) is the Small case at $t = 63$s. Shear instabilities form along the boundary between the bolus and the top layer of the fluid.

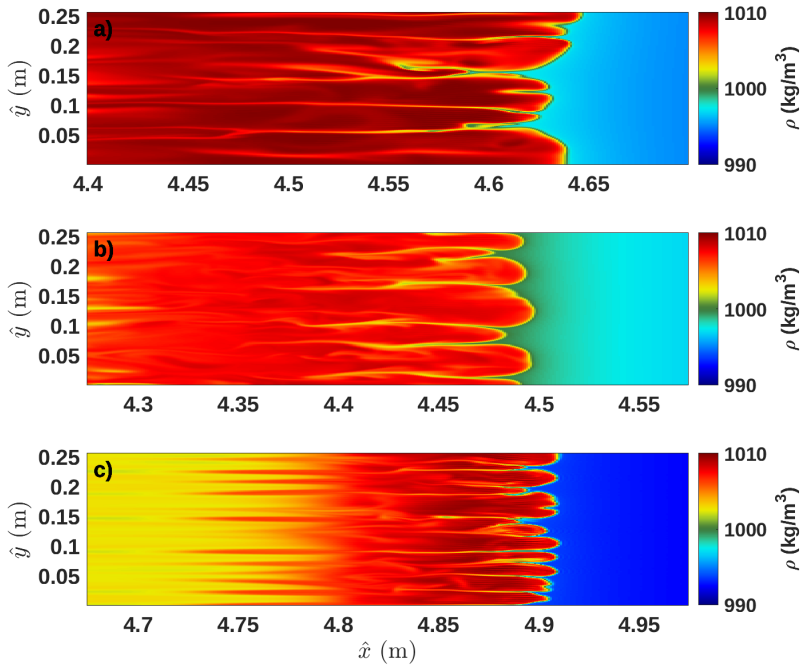

Figure 3.21: The cross-section of the density field at $z = 4.1$mm for each case. a) is the Large case at $t = 59$s, b) is the Medium case at $t = 57$s, and c) is the Small case at $t = 63$s. As the bolus approaches and travels past the attachment point of the pycnocline, it begins to behave as a gravity wave and develops lobe-cleft instabilities.

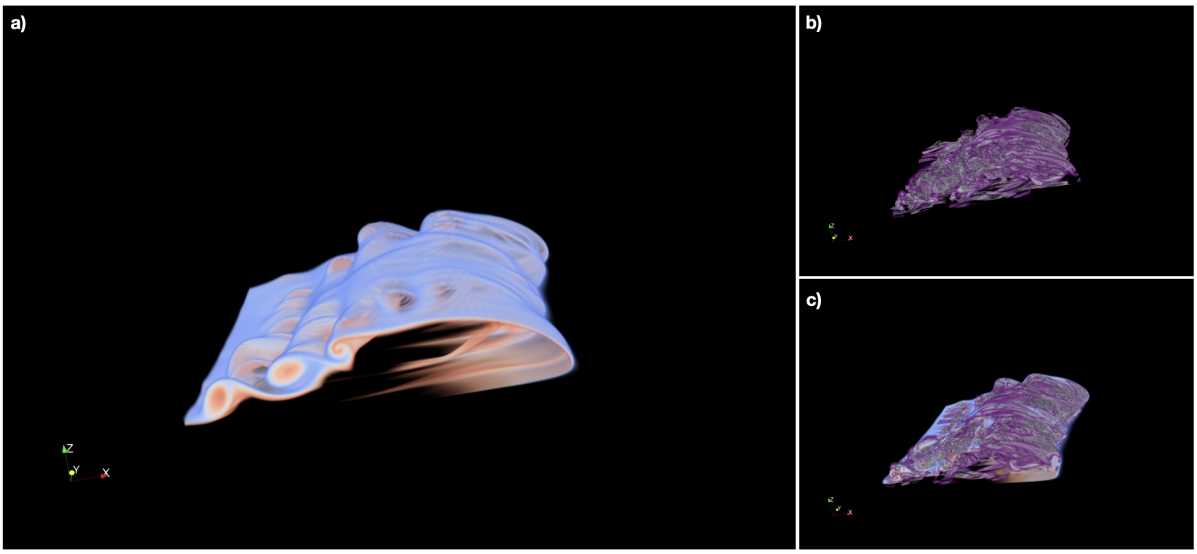

Figure 3.22: Three-dimensional, volumetric depictions of the pycnocline about the leading bolus and regions where $\lambda_2 < -0.0002$ (i.e., λ_2–vortex fields) about the leading bolus at $t = 60$s. These volumes are visualized with the same colorings used in Figure 3.13, but with different opacity maps. Once again, in the density field red indicates a larger density, and blue indicates a lower density; in the λ_2 plots, magenta regions indicate lower-order instabilities ($\lambda_2 \approx -0.0002$) and green regions indicate higher-order instabilities ($\lambda_2 \to -\infty$). a) is solely the pycnocline, b) is solely the vortex field, and c) is the vortex field superimposed on the pycnocline.

3.4 Summary

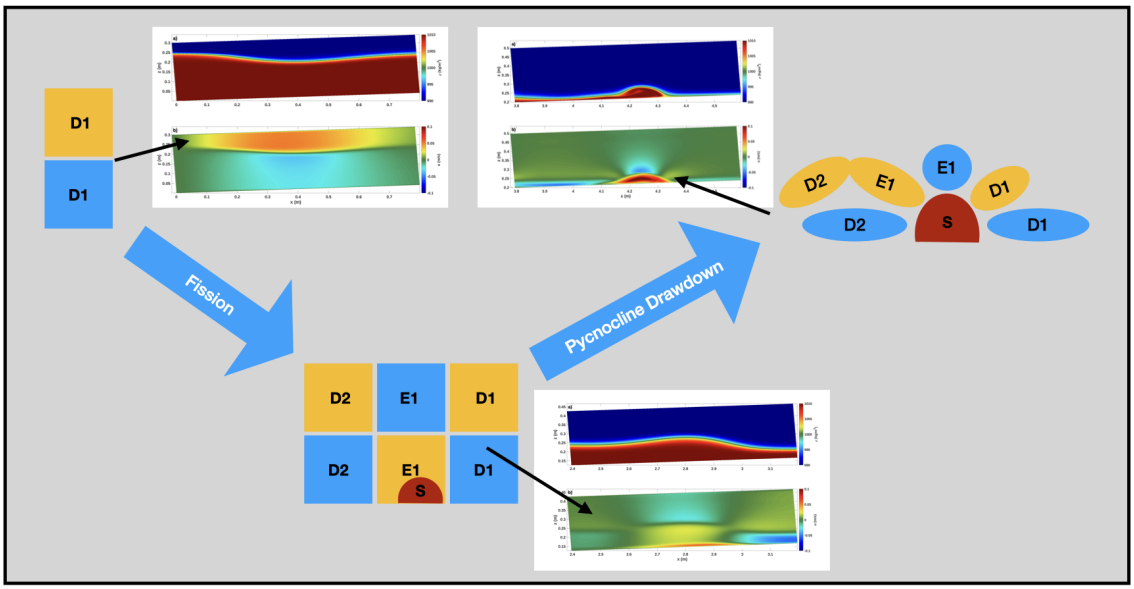

Figure 3.23: An idealization of the evolution of the streamwise velocity field during shoaling. The letters 'D' and 'E' denote currents from waves of depression and elevation, respectively; the number indicates the order of the wave (e.g., E2 is the second wave of elevation). The red bubble with an 'S' represents the separation bubble. Warm (cool) colours indicate prograde (retrograde) motion. Each idealized stage is paired with vertical cross-sections ($y = 0.128$m) of the u and ρ fields from the Small case at representative times (in counter-clockwise order, $t = 4s$, at $t = 35s$, and at $t = 51s$.)

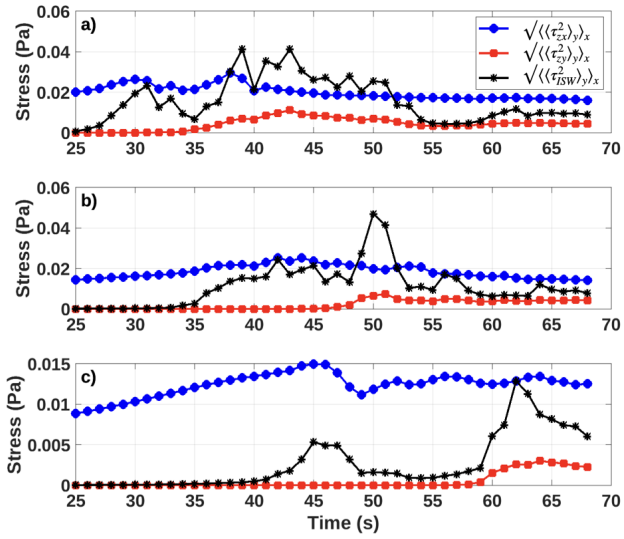

Figure 3.24: Time series of the root-mean square of various bed stresses, where the average is performed over the whole domain. a) is the Large case, b) is the Medium case, and c) is the the Small case.

In the fission regime, a shoaling ISW-D steepens, fissions near the turning point, and then degenerates into a series of boluses. These inviscid processes change how the wave interacts with the viscous BBL, and thus each can be paired with their own qualitatively distinct instability[4]. This process is depicted in Figure 3.1 for the density field, and an idealized version of the shoaling process (which includes the viscous formation of the separation bubble) is depicted in Figure 3.23 for the streamwise velocity field; this latter figure shows the fissioning of the ISW-D into a train of NL waves, followed by the growth of the internal separation bubble, and the subsequent transformation by deformation of the first three nonlinear waves into the first bolus. Another perspective on the overall process is given by Figure 3.24, which shows, for each case, the time series of the domain-averaged bed stresses. Note, in panel c), the independent spikes in the mean τ_{ISW} corresponding to internal separation bubble formation and bolus degeneration. Similar spikes also appear in panels a) and b), though the first group of spikes in each time series (corresponding to internal bubble formation and separation bubble bursting) is much larger due to the presence separation bubble bursting. With this broad overview of the shoaling process in

[4]The degeneration of the wave by boluses corresponds to two instabilities, but they are concurrent (in agreement with experiments by Ghassemi et. al. [17]) and can be treated as a conceptual unit.

the fission regime in mind, a summary of the chapter is presented below.

The first instability, the trailing prograde jet, never generates any secondary instabilities, and consequently remains two-dimensional as the wave approaches the turning point. When the leading ISW-D fissions, its streamwise velocity field provides an adverse shear current that interacts with the currents of the leading ISW-E, as is depicted in Figure 3.23. In the BBL, the interacting currents 'pinch' the front of the prograde jet, and subsequently generate a separation bubble with a prograde current that sits near the front of the leading ISW-E. As a result of the pinch, the along-slope length scale of the separation bubble is smaller than its vertical length scale. The bubble will continue to grow as the wave shoals, and it will come to occupy more space under the leading ISW-E; this can also be seen in Figure 3.23. Eventually, as the pycnocline is drawn towards the bed as the wave approaches the interaction point, this growing bubble will displace the currents from the nonlinear waves, transforming the patches of the streamwise velocity field of the first three ISWs into the velocity field that surrounds the bolus (see the leftmost part of Figure 3.23).

Returning focus to the jet phase, note that after the pinch, the back portion of the jet no longer travels with the wave-train, and remains behind the turning point, where it is modulated into alternating patches of prograde and retrograde current by the wave-train. It is tempting to think that this region of alternating current could produce the sand waves observed by Ma et. al. [30], but the magnitudes of the currents in the modulated region are approximately 1 order of magnitude less than the streamwise currents of the leading wave and the separation bubble (see Figure 3.4), and it is uncertain how this disparity would scale up to a shoaling system in the field.

The interaction between the BBL and the currents within the separation bubble generates smaller internal separation bubbles with retrograde currents; the opposing currents, which have negligible transverse variation, produce two-dimensional vortices. The formation of the internal bubbles produces the first spikes in ejection stress in Figure 3.24. The shear across the boundary of the internal bubble—which varies with the amplitude of the initial wave and thus with Re_{ISW}—determines the strength of the induced vortices. In turn, the strength of the vortices determines the strength of the induced transverse currents, and thereby the significance and magnitude of spanwise variation. In all cases, the vortex interacts with the pycnocline, but only a sufficiently strong vortex can induce baroclinic vortices via overturning. The Large and Medium cases both produce sufficiently strong vortices, but in the Small case, the draw-down produces nothing more than weak entrainment of a bottom sliver of the pycnocline and a small mode-2 disturbance in the pycnocline that propagates downslope. When present, the baroclinic overturning is analagous to the advective breaking observed in the plunging and collapsing regimes; however, in those larger-Ir regimes, the breakdown of the wave is due to inviscid, nonlinear steepening

(i.e., 'breaking') as opposed to vortices generated by a BBL instability.

In the present experiments, the roll-up of the pycnocline, when it occurs, is initially two-dimensional, but both the original and the baroclinic vortices quickly generate transverse currents and the complex structures; examples of the complex structures from the Large case can be seen in Figures 3.12 and 3.13. When the roll-up is present (i.e., in the Medium and Large cases) vigorous stirring of the pycnocline results in mixing in addition to the largest spikes in both ejection stress and transverse bed stress across cases (see panels a) and b) of Figure 3.24). Hence, these systems and their vortices have a significant potential to resuspend sediment behind the leading wave, near the turning point. That being said, only the potential for sediment advection can be discussed, and it is not impossible to believe that even the Medium case may have trouble advecting sediment with sufficiently large and dense grains. This is a rich vein for future investigtion, thought this will be discussed in more detail in Section 4.2.

The primary vortices are local instabilities, which means they travel downslope after they are shed by the leading wave. However, remnants of spanwise currents and high-order vortices are trapped underneath the leading wave, and they will become part of the trapped core of the bolus; i.e., they will determine the initial degree of turbulence inside the bolus. This is consistent with the experimental findings of Moore et. al. [32], which state that the qualitative nature of the flow within the bolus is affected by the currents produced during the breakdown of the parent wave. Adding some detail to this narrative, the present investigation has found that as the leading ISW–E transforms into a bolus, the trapped vortices slowly dissipate. Thereafter, a qualitatively distinct three–dimensionalization occurs: dense fluid leaks out of the rear face and induces circulation within the bolus; the resultant entrainment of the inner bolus boundary by the circulation, alongside longitudinal rolls from lobe-cleft instabilities and billows from shear instabilities along the bolus boundary, ultimately lead to the degeneration of the bolus. Mixing across the bolus boundary is minimal during the degeneration, and the bottom stresses are relatively small compared to those produced during bursting and overturning (Figure 3.24). Thus, a fission–regime bolus can, at most, contribute to cross–bed transport and sediment deposition along the bottom boundary [34]. This is in stark contrast to the vigorous overturning of, and mixing across, the pycnocline during the bursting of the separation bubble.

Chapter 4

Conclusions, and Future Work

4.1 Conclusions

The narrative regarding quasi–two–layer, linear–slope systems in the fission regime can be distilled to the following conclusions: i) if a fissioning wave breaks down it does not break down due to inviscid nonlinear wave processes, but rather due to baroclinic vortices induced by secondary BBL instabilities; ii) the wave evolution is largely two-dimensional until the pycnocline is overturned by baroclinic vortices; iii) three-dimensionalization of the flow occurs twice due to qualitatively distinct mechanisms (once shortly after separation bubble bursting, and once during bolus degeneration); iv) given a sufficiently large Re_{ISW}, separation bubble bursting generates large, turbulent vortices that overturn the pycnocline between the turning point and the interaction point; and, finally, v) the bolus is not a significant source of cross-layer mixing. The significance of these conclusions is elucidated by the context from the results of other linear–slope shoaling investigations.

As mentioned in Chapter 1, the shallow-slope fission regime has been somewhat unexplored by numericists due to computational cost: to observe a wave shoal into a bolus over realistically shallow slopes ($\theta \in [\pi/180, \pi/30]$) requires long domains ($L_x = O(10)$m). Recent numerical work on the Fission regime has therefore employed moderate resolution in three dimensions [4, 33], or high resolution in two dimensions [46]. These works have reported conclusions similar to i), ii), and v). The work in this thesis is distinguished by using a fine resolution[1] in three dimensions, and by probing the fission regime over a range of amplitudes ($H \in [10\text{cm}, 20\text{cm})$. That is, this investigation provides detailed, mecha-

[1] approximately 1mm

nistic insights into the previously known conclusions, because the BBL is well-resolved[2] which allows for the observations of initially small BBL instabilities, their growing spanwise variations, and how they interact with the bulk currents. Additionally, by accessing the Small case through varying the amplitude, this investigation has found that the separation bubble does not always burst (conclusion iv)), and that the bolus three-dimensionalizes independently of separation bubble bursting and the subsequent pycnocline overturning (conclusion iii)).

All linear–slope systems follow the general pattern of wave–incidence, wave breakdown near the turning point, and bolus formation between the turning point and the interaction point [1, 2, 4, 7, 17, 20, 27, 33, 46]. The systems are phenomenologically differentiated by the qualitative mechanisms of breaking, and parametrically differentiated by wave slope (S_w), shore slope ($S = \tan\theta$), and Re_{ISW} [2, 4, 7, 33]. Ir (the ratio of S to S_w) measures, to first order, the degree to which incident wave energy is reflected or transmitted. When Ir is large, the interaction between reflected and incident wave energy causes advective breaking of the wave [2]; but, when it is small ($Ir \lesssim O(0.1)$), the wave self-interaction causes the main wave to fission, and breakdown occurs only if BBL instabilities generate barotropic vortices. In quasi–two–layer systems, Aghsaee et. al. [2] identified the advective regimes (in order of decreasing Ir) of surging, plunging, and collapsing; they also noted the presence of fissioning waves, which are not overturned by their own currents. In the surging regime, the majority of wave energy is reflected, and the remaining transmitted energy immediately forms a bolus; large billows can be produced during this process [4, 33] which have the potential mix fluid across the pycnocline. In the plunging regime, less energy is reflected and the wave breaks backwards before forming a bolus (hence, Moore et. al. label these waves 'back-breakers'). Waves in the collapsing regime are similar, but they break forward. Regardless, plunging and collapsing regime waves advectively overturn the pycnocline, greatly increasing the cross-layer mixing [2, 4, 32]. Conversely, fissioning waves have been observed to evolve gently without overturning, and were thus overlooked as a source of significant mixing [2]. However, recent investigations highlight how structures produced by BBL instabilities[3] (specifically, separation bubble bursting) can induce mixing across the pycnocline via vortices [4, 46]. Indeed, the present investigation shows that, given a sufficiently large Re_{ISW}, vortices from BBL instabilities vigorously overturn the pycnocline with potentially significant mixing, and large spikes in bed stresses near the turning point.

When bursting can occur, latent spanwise variation (which manifests as $O(10^{-6})$m/s

[2]The only "moderately" resolved portions of the domain are near the pycnocline, and even then this only is true during extreme thinning during overturning and bolus degeneration.

[3]Note that Athur and Fringer did not attribute these structures to BBL instabilities [4].

alternating patches in the v field in the separation bubble) is amplified by the dominant two-dimensional shear currents about the boundary of the internal separation bubble, and later by the initially two-dimensional roll-up of the pycnocline. This is consistent with the findings of Sakai et. al. [36]: they observed that vortex shedding events were preceded by alternating patches of streamwise vorticity that were excited by shear along a prograde jet in the BBL over a flat–bottom (i.e., untilted) system. Spanwise variation is instigated a second time during bolus degeneration. In case 0p5A—which did not exhibit bursting—the initially two-dimensional shear current about the top boundary of the bolus, and the intially two-dimensional circulating current produced by the leaking core of the bolus, excited three-dimensional motion. The only three-dimensional structures not produced by two-dimensional motion exciting latent three-dimensional modes were the lobe-cleft instabilities; they were instead produced by buoyant plumes once the bolus passed the the interaction point, placing its relatively dense core over relatively light fluid from the upper slope. In a model that augmented SPINS with a sediment model, Olsthoorn and Stastna [34] observed sediment resuspension to occur before three-dimensionalization of their systems, which suggests that the intially two-dimensional barotropic vortex, i.e. the breakdown event between the turning point and the interaction point, has the greatest potential to resuspend sediment.

What does this mean for energy and sediment dynamics in a geophysical context? Hartharn-Evans et. al. [20] showed that the plunging regime, and both the plunging and collapsing regimes, are inaccessible for surface stratifications, and broad-tanh stratifications, respectively. Accordingly, since the coastal shelf slope is quite shallow [7], and since the coastal shelf typically has a stratification dominated by a near-surface pycnocline (with a mixed layer immediately adjacent to the surface) [27], fissioning and collapsing waves would likely be the sole source of overturning in the upper water column. Additionally, for a shallow slope, only extremely small-amplitude ISWs would populate the collapsing regime; thus, the correspondingly small Re_{ISW} suggests that the resulting currents would be unlikely to induce turbulence and associated mixing, or to induce bottom stresses sufficiently strong for sediment resuspension (although, they could still induce cross-bed transport) [34]. The capability of fissioning waves to induce overturning events is therefore vital to the narrative that shoaling ISWs significantly contribute to turbulent mixing and sediment resuspension on the coastal shelf [7]. Arthur and Fringer [4] note that bolus degeneration and propagation produces significantly less mixing and dissipation than wave breakdown. In fact, they found that bulk mixing and dissipation of the system could be well-approximated by the equivalent local measures at a point between the turning point and the breaking point[4] [4]. Therefore, if fissioning waves were unable

[4] As noted by Ghassemi et. al. [17], the breaking point is downslope of the interaction point.

to generate strong mixing across the pycnocline and turbulence via BBL instabilities, then shoaling ISWs would only be able to transport sediment via the leaking core of a bolus.

4.2 Future Work

The phrases "potential for mixing" and "potential for sediment resuspension," and their sentiments, are repeated extensively throughout this thesis. Inferring mixing and sediment transport capability from bottom stresses, vortex fields, currents, and the results of other studies is certainly a valid approach, but such claims ultimately must be verified with quantitative results from numerical experiments. This raises the question: "why did the present investigation neglect sediment–coupling and mixing calculations?" First, the primary focus of the investigation was the degree of significance and presence of spanwise variation in a shallow-slope system as wave-amplitude (and hence the tendency for turbulence) was varied. This in itself is a large topic, and could inform the design of simulations investigating sediment-coupling and mixing.

Second, the possible variations of experiments with sediment–coupled models could yield several theses alone. The approach of Stastna and Olsthoorn is relatively straightforward to implement in SPINS, but the additional computational cost of resolving the sediment field would have made simulating a three-dimensional fission regime system, with a Re_{ISW} that allows for bursting, prohibitively computationally expensive. Their method also only applies to fine–grain sediment. As noted by Ma et. al. [30], the sediment beds where sand waves are observed are often composed of course–grain sediment, and would need a more complicated model, such as a Shields model, or a Lagrangian particle-tracking method, to investigate. An immediate extension of the present investigation, and motivated by the investigation by Hartharn-Evans et. al. [20], would be to use i) a more oceanically relevant stratification, and ii) the model of Stastna and Olsthoorn to observe the lab-scale dynamics of sediment clouds (a.k.a. nepheloid layers) as the pycnocline is adjusted. Such a model would require perhaps twice the resolution in the z-grid (and thus approximately twice the resources) to resolve sediment clouds in the middle to upper water column; a necessarily small mass diffusivity would further increase the cost.

Third, the exponential filter used by SPINS was unable to suppress ringing during certain portions of the evolutions where the density interfaces thinned (i.e., during pycnocline overturning and bolus degeneration). Though ringing did not significantly affect the bulk evolution of the system, it would obfuscate any mixing calculations based on the sorting algorithm of Winters et al [44]. The most immediate solution to this problem would be to increase the vertical and streamwise resolutions. Unfortunately, as mentioned in Chapter

2, the vertical no-slip boundary condition requires the use of a Chebyshev grid, and increasing the vertical resolution therefore comes with diminishing returns. More precisely, the Chebyshev grid bunches points near the vertical boundaries, and spaces them out in the middle of the water column; as such, choosing a grid so that the tank interior has sufficiently many points to resolve small features at all times therefore increases the number of points near the boundaries many times over—meaning that the computational cost can become very expensive very easily.

An alternative solution to increasing the resolution, is to repeat the experiments from this thesis with stronger filter parameters, or with hyperviscosity in lieu of an exponential filter; then, it is possible to draw conclusions about mixing and dissipation by comparing the trends in these variables across cases with different filters or hyperviscosity. In any case, this approach is a significant undertaking. The experiments in this thesis each took under two weeks to complete on the ComputeCanada Graham cluster; each run used 256 parallel processes and 512GB of memory to produce 44 outputs for 4 fields. As such, repeating the experiments with 2 filter variations would require approximately 12 weeks of computational time, 1536 processes, and 3072GB of memory. This does not account for secondary computations needed to calculate local and bulk mixing and dissipation.

References

[1] Payam Aghsaee and Leon Boegman. Experimental investigation of sediment resuspension beneath internal solitary waves of depression. *Journal of Geophysical Research: Oceans*, 120(5):3301–3314, 2015.

[2] Payam Aghsaee, Leon Boegman, and Kevin G Lamb. Breaking of shoaling internal solitary waves. *Journal of Fluid Mechanics*, 659:289–317, 2010.

[3] R. A. Antonia. Conditional sampling in turbulence measurement. *Annual review of fluid mechanics*, 13(1):131–156, 1981.

[4] Robert S Arthur and Oliver B Fringer. The dynamics of breaking internal solitary waves on slopes. *Journal of fluid mechanics*, 761:360–398, 2014.

[5] Robert S Arthur and Oliver B Fringer. Transport by breaking internal gravity waves on slopes. *Journal of Fluid Mechanics*, 789:93–126, 2016.

[6] G. K. Batchelor. *An Introduction to Fluid Dynamics*. Cambridge Mathematical Library. Cambridge University Press, 2000.

[7] Leon Boegman and Marek Stastna. Sediment resuspension and transport by internal solitary waves. *Annual review of fluid mechanics*, 51:129–154, 2019.

[8] John P Boyd. *Chebyshev and Fourier spectral methods*. Courier Corporation, 2001.

[9] Magda Carr and PA Davies. Boundary layer flow beneath an internal solitary wave of elevation. *Physics of Fluids*, 22(2):026601, 2010.

[10] Magda Carr, Peter A Davies, and Pruthvi Shivaram. Experimental evidence of internal solitary wave-induced global instability in shallow water benthic boundary layers. *Physics of Fluids*, 20(6):066603, 2008.

[11] M. S. Chong, A. E. Perry, and B. J. Cantwell. A general classification of three-dimensional flow fields. *Physics of Fluids A: Fluid Dynamics*, 2(5):765–777, 1990.

[12] Anqing Cui. *On the parallel computation of turbulent rotating stratified flows*. Stanford University, 1999.

[13] P. A. Davidson. *Turbulence: an introduction for scientists and engineers*. Oxford university press, 2015.

[14] Peter J Diamessis and Larry G Redekopp. Numerical investigation of solitary internal wave-induced global instability in shallow water benthic boundary layers. *Journal of physical oceanography*, 36(5):784–812, 2006.

[15] Y. Dubief and F. Delcayre. On coherent-vortex identification in turbulence. *Journal of Turbulence*, 1:N11, 2000.

[16] OB Fringer, M Gerritsen, and RL Street. An unstructured-grid, finite-volume, nonhydrostatic, parallel coastal ocean simulator. *Ocean modelling*, 14(3-4):139–173, 2006.

[17] Amin Ghassemi, Saeid Zahedi, and Leon Boegman. Bolus formation from fission of nonlinear internal waves over a mild slope. *Journal of Fluid Mechanics*, 932, 2022.

[18] Taylor Hanson, Marek Stastna, and Aaron Coutino. Stratified shear instability in the cabbeling regime. *Physical Review Fluids*, 6(8):084802, 2021.

[19] Carlos Härtel, Fredrik Carlsson, and Mattias Thunblom. Analysis and direct numerical simulation of the flow at a gravity-current head. part 2. the lobe-and-cleft instability. *Journal of Fluid Mechanics*, 418:213–229, 2000.

[20] Samuel G Hartharn-Evans, Magda Carr, Marek Stastna, and Peter A Davies. Stratification effects on shoaling internal solitary waves. *Journal of Fluid Mechanics*, 933, 2022.

[21] Karl R Helfrich and W Kendall Melville. Long nonlinear internal waves. *Annu. Rev. Fluid Mech.*, 38:395–425, 2006.

[22] Wray A. A. Hunt J. C. R. and Moin P. Eddies, streams, and convergence zones in turbulent flows. In *Proceedings of CTR-S88*. NASA, December 1988.

[23] Christopher Jackson. Internal wave detection using the moderate resolution imaging spectroradiometer (modis). *Journal of Geophysical Research: Oceans*, 112(C11), 2007.

[24] J. Jeong and F. Hussain. On the identification of a vortex. *Journal of Fluid Mechanics*, 285:69–94, 1995.

[25] M. Jiang, R. Machiraju, and D. Thompson. Detection and visualization of vortices. In C.D. Hansen and C.R. Johnson, editors, *Visualization Handbook*, chapter 14. Elsevier Science, 2011.

[26] P.K. Kundu and I.M. Cohen. *Fluid Mechanics*. Elsevier Science, 2010.

[27] Kevin G Lamb. Internal wave breaking and dissipation mechanisms on the continental slope/shelf. *Annual Review of Fluid Mechanics*, 46:231–254, 2014.

[28] Mike R Leeder. *Sedimentology and sedimentary basins: from turbulence to tectonics*. John Wiley & Sons, 2009.

[29] M. Lesieur. *Turbulence in Fluids*. Fluid Mechanics and Its Applications, 84. Springer Netherlands, Dordrecht, 4th ed. 2008. edition, 2008.

[30] Xiaochuan Ma, Jun Yan, Yijun Hou, Feilong Lin, and Xufeng Zheng. Footprints of obliquely incident internal solitary waves and internal tides near the shelf break in the northern s outh c hina s ea. *Journal of Geophysical Research: Oceans*, 121(12):8706–8719, 2016.

[31] John Marshall, Alistair Adcroft, Chris Hill, Lev Perelman, and Curt Heisey. A finite-volume, incompressible navier stokes model for studies of the ocean on parallel computers. *Journal of Geophysical Research: Oceans*, 102(C3):5753–5766, 1997.

[32] Christine D Moore, Jeffrey R Koseff, and Erin L Hult. Characteristics of bolus formation and propagation from breaking internal waves on shelf slopes. *Journal of Fluid Mechanics*, 791:260–283, 2016.

[33] Keisuke Nakayama, Takahiro Sato, Kenji Shimizu, and Leon Boegman. Classification of internal solitary wave breaking over a slope. *Physical Review Fluids*, 4(1):014801, 2019.

[34] Jason Olsthoorn and Marek Stastna. Numerical investigation of internal wave-induced sediment motion: Resuspension versus entrainment. *Geophysical Research Letters*, 41(8):2876–2882, 2014.

[35] John Scott Russell. *Report on Waves: Made to the Meetings of the British Association in 1842-43*. 1845.

[36] Takahiro Sakai, Peter J Diamessis, and Gustaaf B Jacobs. Self-sustained instability, transition, and turbulence induced by a long separation bubble in the footprint of an internal solitary wave. i. flow topology. *Physical Review Fluids*, 5(10):103801, 2020.

[37] Edward A Spiegel and G Veronis. On the boussinesq approximation for a compressible fluid. *The Astrophysical Journal*, 131:442, 1960.

[38] Marek Stastna and Kevin G Lamb. Large fully nonlinear internal solitary waves: The effect of background current. *Physics of fluids*, 14(9):2987–2999, 2002.

[39] C. Subich. *Simulation of the Navier-Stokes Equations in Three Dimensions with a Spectral Collocation Method*. The University of Waterloo, 2011.

[40] Lloyd N Trefethen. *Spectral methods in MATLAB*. SIAM, 2000.

[41] Leo C Van Rijn et al. *Principles of sediment transport in rivers, estuaries and coastal seas*, volume 1006. Aqua publications Amsterdam, 1993.

[42] SK Venayagamoorthy and OB Fringer. Numerical simulations of the interaction of internal waves with a shelf break. *Physics of Fluids*, 18(7):076603, 2006.

[43] BC Wallace and DL Wilkinson. Run-up of internal waves on a gentle slope in a two-layered system. *Journal of Fluid Mechanics*, 191:419–442, 1988.

[44] Kraig B Winters, Peter N Lombard, James J Riley, and Eric A D'Asaro. Available potential energy and mixing in density-stratified fluids. *Journal of Fluid Mechanics*, 289:115–128, 1995.

[45] J.C. Wyngaard. *Turbulence in the Atmosphere*. Cambridge University Press, 2010.

[46] Chengzhu Xu and Marek Stastna. Instability and cross-boundary-layer transport by shoaling internal waves over realistic slopes. *Journal of Fluid Mechanics*, 895, 2020.

[47] Chengzhu Xu, Christopher Subich, and Marek Stastna. Numerical simulations of shoaling internal solitary waves of elevation. *Physics of Fluids*, 28(7):076601, 2016.